CSIRO PUBLISHING

Journal of Southern Hemisphere Earth Systems Science, 2020, **70**, 225–251
https://doi.org/10.1071/ES19040

Configuration and spin-up of ACCESS-CM2, the new generation Australian Community Climate and Earth System Simulator Coupled Model

Daohua Bi[A,I], *Martin Dix*[A], *Simon Marsland*[A,B,C], *Siobhan O'Farrell*[A], *Arnold Sullivan*[A], *Roger Bodman*[D], *Rachel Law*[A], *Ian Harman*[E], *Jhan Srbinovsky*[A], *Harun A. Rashid*[A], *Peter Dobrohotoff*[A], *Chloe Mackallah*[A], *Hailin Yan*[F], *Anthony Hirst*[F], *Abhishek Savita*[A,B,C], *Fabio Boeira Dias*[A,B,C], *Matthew Woodhouse*[A], *Russell Fiedler*[G] *and Aidan Heerdegen*[C,H]

[A]CSIRO Oceans and Atmosphere, 107–121 Station Street, Aspendale, Vic. 3195, Australia.
[B]Institute for Marine and Antarctic Studies, University of Tasmania, Hobart, Australia.
[C]ARC Centre of Excellence for Climate Extremes, Sydney, Australia.
[D]University of Melbourne, Melbourne, Australia.
[E]CSIRO Oceans and Atmosphere, Canberra, Australia.
[F]Bureau of Meteorology, Melbourne, Australia.
[G]CSIRO Oceans and Atmosphere, Hobart, Australia.
[H]Australian National University, Canberra, Australia.
[I]Corresponding author. Email: Dave.Bi@csiro.au

Abstract. A new version of the Australian Community Climate and Earth System Simulator coupled model, ACCESS-CM2, has been developed for a wide range of climate modelling research and applications. In particular, ACCESS-CM2 is one of Australia's contributions to the World Climate Research Programme's Coupled Model Intercomparison Project Phase 6 (CMIP6). Compared with the ACCESS1.3 model used for our CMIP5 submission, all model components have been upgraded as well as the coupling framework (OASIS3-MCT) and experiment control system (Rose/Cylc). The component models are: UM10.6 GA7.1 for the atmosphere, CABLE2.5 for the land surface, MOM5 for the ocean, and CICE5.1.2 for the sea ice. This paper describes the model configuration of ACCESS-CM2, documents the experimental set up, and assesses the model performance for the preindustrial spin-up simulation in comparison against (reconstructed) observations and ACCESS1.3 results. While the performance of the two generations of the ACCESS coupled model is largely comparable, ACCESS-CM2 shows better global hydrological balance, more realistic ocean water properties (in terms of spatial distribution) and meridional overturning circulation in the Southern Ocean but a poorer simulation of the Antarctic sea ice and a larger energy imbalance at the top of atmosphere. This energy imbalance reflects a noticeable warming trend of the global ocean over the spin-up period.

Keywords: ACCESS-CM2, climate change, climate simulation, CMIP6, coupled climate model, evaluation, greenhouse gases, physical configuration, preindustrial spin-up, tuning and debugging.

Received 20 December 2019, accepted 29 June 2020, published online 8 October 2020

1 Introduction

Coupled climate models play a crucial role in climate variability and climate change research. Importantly, they are used to simulate climate change processes and to project the future state of the global climate system under various scenarios of increasing concentrations of greenhouse gases. The Coupled Model Intercomparison Project phase 5 (CMIP5) (Taylor *et al.* 2012) was the most recent joint effort of the world climate modelling community to compare coupled climate model simulations to better understand historical and future climate changes.

The Australian Community Climate and Earth System Simulator coupled model versions 1.0 and 1.3 (ACCESS1.0, ACCESS1.3; Bi *et al.* 2013*b*) participated in this international effort and provided Australia's major model input to the Fifth Assessment Report of the Intergovernmental Panel on Climate Change (IPCC AR5). International model evaluation studies (e.g. Flato *et al.* 2013; Sillmann *et al.* 2013; Watterson *et al.* 2013) showed that the ACCESS simulations were among the better performing of the CMIP5 simulations, and were particularly skilful over Australia, based on a set of key climatic fields

obtained from the historical simulations. The model output fields from the ACCESS CMIP5 simulations (Dix *et al.* 2013), including the historical run and projections for the 21st century have been placed on the Earth System Grid Federation (ESGF; Cinquini *et al.* 2014) data distribution system node based at Australia's National Computational Infrastructure, where it is still being accessed by the global research community.

Internationally, climate models are continually being enhanced through increasing resolution and improved process representation. For ACCESS, recent development has focussed on building ACCESS-ESM1 (Law *et al.* 2017) and ACCESS-ESM1.5 (Ziehn *et al.* 2020) to include the carbon cycle, and configuring a new generation physical climate model (ACCESS-CM2). The immediate goal of ACCESS-CM2 and ACCESS-ESM1.5 is participation in CMIP6 (Eyring *et al.* 2016) which is the current successor to CMIP5. CMIP6 features an extensive set of sub-projects targeting model evaluation, the understanding of fundamental processes, and the updating of projections. ACCESS-CM2 has been developed over a number of years and through several prototype versions. In particular, we tested several atmospheric model configurations and two land surface models, as well as a higher resolution ocean configuration. Here we will only focus on the configurations that have contributed to the spin-up of the model for CMIP6 simulations.

This paper provides brief descriptions of all model components in Section 2 and a brief review of experimental design, parameter tuning, and spin-up processes in Section 3. We evaluate the model performance in Section 4 by presenting results of the multi-century preindustrial (PI) spin-up simulation compared against (mostly) recent observations where applicable and the results of one of our CMIP5 models, ACCESS1.3. We summarise in Section 5, discussing the model skills and deficiencies. More detailed and specific analyses of the ACCESS-CM2 CMIP6 experiments will be presented in companion papers.

2 Model description

ACCESS-CM2, as used for CMIP6, comprises the following components: UM10.6 GA7.1 configuration for the atmosphere; the Community Atmosphere Biosphere Land Exchange (CABLE) model version 2.5 (coupled directly to the UM) for the land surface; CICE5.1.2 for the sea ice; MOM5 for the ocean; OASIS3-MCT for the numerical coupler; and the Rose/Cylc (Oliver *et al.* 2019) framework for experiment management such as model configuration and simulation control. Since all the sub-models have been well documented by their individual developers, we provide brief descriptions, mainly documenting the major changes occurring in the scientific configurations of the model components since the implementation of our CMIP5 model ACCESS1.3.

2.1 Atmosphere: UM

The atmospheric component of the ACCESS coupled model, the Met Office Unified Model (UM), has been upgraded from a UM vn7.3 configuration, which had atmospheric physics close to GA1.0 (Arribas *et al.* 2011; Hewitt *et al.* 2011) for ACCESS1.3 (Bi *et al.* 2013*b*), to the UM vn10.6 GA7.1 configuration (Walters *et al.* 2019) for ACCESS-CM2.

2.1.1 Grid, resolution, and dynamics

The UM uses a regular longitude-latitude grid with Arakawa C-grid staggering (Arakawa and Lamb 1977) horizontally, and terrain-following hybrid height coordinates with the vertical Charney-Phillips staggering (Charney and Phillips 1953). The available computational resources meant that for CMIP6, ACCESS-CM2 is configured with the same horizontal resolution as ACCESS1.3 (1.25° latitude by 1.875° longitude corresponding to a grid resolution of approximately 135 km in mid-latitude). However, compared with the vertical 38-level (with a top at 40 km) configuration of GA1 for ACCESS1.3, the GA7.1 implementation for ACCESS-CM2 has a substantially enhanced vertical resolution of 85 levels (50 below 18 km and 35 above, with a much higher top at 85 km). In particular, stratospheric resolution is improved.

The UM in GA7.1 uses the new "ENDGame" dynamical core (Wood *et al.* 2014) rather than the "New Dynamics" (Davies *et al.* 2005) used in earlier versions. It uses a semi-implicit semi-Lagrangian formulation to solve the non-hydrostatic equations of motion (Wood *et al.* 2014). Details of the changes to the dynamics, and the resulting improvements of ENDGame over New Dynamics, have been presented in Wood *et al.* (2014) and Walters *et al.* (2017) among others.

2.1.2 Physical parameterisations

The atmospheric physical parameterisations in UM GA7.1 are fully documented in Walters *et al.* (2019), and ACCESS-CM2 uses an identical implementation. Here we provide a brief summary and, where appropriate, highlight differences from ACCESS1.3.

GA7.1 uses the SOCRATES radiative transfer scheme (Edwards and Slingo 1996; Manners *et al.* 2015) with a new configuration. Shortwave and longwave radiation calculations use 6 and 9 bands respectively (see Table 1 of Walters *et al.* 2019). The full radiation calculations in ACCESS-CM2 are done every hour using the instantaneous cloud fields and a mean solar zenith angle for the following one-hour period. The radiation scheme in ACCESS1.3 was similar to that of GA1 but modified to include the "Tripleclouds" scheme of Shonk and Hogan (2008) to represent horizontal cloud inhomogeneity, as described by Sun *et al.* (2013). The radiative time step was 3 hours in ACCESS1.3.

The unresolved turbulent motions in the atmospheric boundary layer are parameterised to obtain the turbulent fluxes of heat, moisture and horizontal momentum using the scheme of Lock *et al.* (2000) with modifications (Lock 2001; Brown *et al.* 2008). ACCESS1.3 used the boundary layer physical parameterisation as in GA1 but with modifications to algorithms for turbulent fluxes at the air-sea interface based on field programs (Fairall *et al.* 2003), which were found to ease certain biases of SST distribution in the global ocean.

In GA7.1, the convection scheme representing the sub-grid scale transport of heat, moisture, momentum, aerosol and gas-phase tracers associated with cumulus clouds within a grid box is a mass flux scheme based on Gregory and Rowntree (1990) with extensions to include down-drafts (Gregory and Allen 1991) and convective momentum transport (CMT; Gregory *et al.* 1997). ACCESS1.3 followed the GA1.0 approach for convection, but

Table 1. PI Spin-up progress and tuning records of ACCESS-CM2j and ACCESS-CM2

ACCESS-CM2j		*ACCESS-CM2*	
Job name and model years	Notes of debugging and tuning efforts (Changes made to setup in a run were carried on to the new run followed unless picked out specifically.)	Job name and model years	Notes of debugging and tuning efforts (Changes made to setup in a run were carried on to the new run followed unless picked out specifically.)
at658 (cold start) 1–200	In MOM, background diffusion reduction in tropical oceans turned on since year 83. In CICE, sea ice albedos were reduced by 5%: albicei = 0.342, albicev = 0.741, which removes the super thick ice in Arctic.		
av630 (warm start from at658) 201–500	In MOM, sea water specific heat capacity changed to 3992.1032 $J\,kg^{-1}\,°C^{-1}$, the pre-TEOS10 recommendation.	ax871 (warm start from at658) 201–300	CABLE in place of JULES for land surface representation, with UM, MOM5 and CICE5 configured the same way as in the CM2j run av630, except the sea ice albedos were using the default values: albicei = 0.36, albicev = 0.78
bb039 501–600	The calculated sea surface (open water) albedo was increased by 2% in attempt to suppress sea surface warm drift. In MOM, shortwave penetration switched to the more sophisticated GFDL scheme. In CICE, sea ice albedos were set back to albicei = 0.36, albicev = 0.78 because the ice becomes too thin.	bd052 301–400	In CABLE, Antarctic and Greenland ice albedo increased to better match satellite observations, snow roughness increased Switched to using PFT dependent LAI derived from NCAR data.
		be106 401–500	With 2% ocean (open water) surface albedo increase.
bc407 601–975	New MOM5 executable (using the "harmonised" ocean code, same as that for ACCESS-OM2). No change in model physics.	bf481 501–850	Switched to harmonised ocean code. Corrected CABLE error related to precipitation and canopy evaporation.
		bi889 851–950	Corrected problem with CABLE 10 m wind speed which is coupled to sea-salt aerosol generation at coastal points. Also fixed error in sea-salt dry deposition related to 9/17 tile mismatch. Corrected calculation of sea salt aerosol density. Removed the 2% increase of ocean albedo as surface temperature evolvement at this stage showed no need for this enhancement.

the CMT was not turned on for deep convection due to a code error inadvertently introduced during testing.

GA7.1 for ACCESS-CM2 uses the prognostic cloud fraction and prognostic condensate (PC2) scheme (Wilson *et al.* 2008) with modifications to the cloud erosion parameterisation (Morcrette 2012), with PC2 representing both convective and large-scale cloud. The GA1.0 implementation of the PC2 scheme used in ACCESS1.3 was modified through use of the parameterisation of Franklin *et al.* (2012) to modify the ice cloud fraction and the cloud area scheme of Boutle and Morcrette (2010) to account for the effects of coarse vertical resolution on low level cloud cover. This Franklin modification is not used in the PC2 scheme for ACCESS-CM2 because of the enhancement in the GA7.1 vertical resolution mentioned above.

Perhaps the most significant change in GA7.1 is the introduction of new prognostic aerosol scheme GLOMAP-mode (Global Model of Aerosol Processes; Mann *et al.* 2010, 2012) which is a component of the wider UK Chemistry and Aerosol (UKCA) code. The CLASSIC (Coupled Large-scale Aerosol Simulator for Studies in Climate) aerosol parameterisation (Bellouin *et al.* 2011) used in ACCESS1.3 (and in all GA versions before GA7.0) is a single-moment mass-based bulk aerosol scheme. In contrast, GLOMAP-mode is a two-moment aerosol scheme, resolving both aerosol mass and number. Thus, aerosol size distributions, composition and optical properties are resolved in a more detailed, physically based manner. The prognostic aerosol species included in GLOMAP-mode are sulfate (SO_4), black carbon (BC), organic carbon (OC) and sea salt (SS), and they are internally mixed within each of five modes (soluble nucleation, Aitken, accumulation and coarse modes, and insoluble Aitken mode). Another important type of aerosol, mineral dust, is not included in the GLOMAP-mode species and is simulated separately using the Woodward (2011) scheme. The effect of stratospheric aerosol from explosive volcanic eruptions uses prescribed optical depths. We note that analysis of ACCESS1.3 CMIP5 simulations (Dix *et al.* 2013) shows essentially zero dust concentration in the model. This was a consequence of changing the land surface scheme to CABLE and freezing the ACCESS1.3

code version for CMIP5 before the dust setting was found to be incomplete. For ACCESS-CM2, the dust is properly included.

2.2 Land surface: CABLE

Millennium-length spin-ups have been conducted using two land surface models (see Appendix 1 for details of these spin-up runs). The first land surface model is the Joint UK Land Environment Simulator (JULES; Best *et al.* 2011; Clark *et al.* 2011), which is embedded in the UM atmospheric model. JULES handles surface fluxes over the model's whole surface domain, not just over land, to calculate surface exchange (vegetation canopies, snow, soils, ocean surface, and sea ice). We use the JULES model in the GL7.0 configuration (Walters *et al.* 2019), and we designate the model spin-up using JULES as ACCESS-CM2j. The second land surface model is CABLE version 2.5 (CABLE2.5). The land-surface exchange within JULES was replaced by CABLE2.5 and a second spin-up was initiated branching from the ACCESS-CM2j spin-up as described in Appendix 1. This second spin-up with CABLE2.5 forms the basis for the ACCESS-CM2 CMIP6 simulations. It should be noted that ACCESS-CM2 continues to utilise JULES representations for some terrestrial processes, particularly dust source/deposition and river routing. ACCESS-CM2 also uses the UM-UKCA-JULES representations for aerosol sources/deposition, and consistency is maintained by passing CABLE derived exchange coefficients to the UM/UKCA in place of the JULES values. Aerosol deposition coefficients were remapped from the best match of the 17 tile types of JULES to the CABLE vegetation types.

CABLE2.5 is an updated version of CABLE1.8 (Kowalczyk *et al.* 2013) used in ACCESS1.3 for CMIP5 submission. The updates are to the code base and configuration, including some changes to parameters and forcing data. A listing of these updates is provided in Harman *et al.* (2019), Section 2, whereas a more comprehensive assessment of the impact of the configuration changes is being prepared for publication. Particular care was taken to ensure that energy was well conserved in the coupling of CABLE to the atmosphere. Likewise, water conservation issues originating at the interface between CABLE and the river routing scheme have also been addressed. For ACCESS-CM2, CABLE is configured to use up to 13 surface tile types, 10 for vegetated and 3 for non-vegetated types, with a variable number of tiles used in each grid-cell defined by prescribed tile fractions. The vegetation distribution is based on that used in ACCESS1.3 for CMIP5, originally derived from Lawrence *et al.* (2012) as described in Kowalczyk *et al.* (2013). The tile fractions do not vary in time, and the 1850 vegetation distribution is used in all CMIP6 simulations. Leaf area index and canopy height are prescribed with a seasonally varying climatology. Canopy height is dependent only on vegetation type, and leaf area index varies spatially and with vegetation type. The variation with vegetation type was not included in ACCESS1.3 and, for ACCESS-CM2, was derived from Lawrence *et al.* (2012). Each tile is modelled with a separate soil column of six layers.

In ACCESS, the atmospheric model land-sea mask, especially coastal points with fractional land, is defined using the ocean model land-sea mask for consistency between the atmosphere-land and ice-ocean subsystems. This ensures conservation of river runoff when it is passed from the UM into CICE (and then to MOM) by the OASIS remapping. The resultant CABLE land fraction is used to scale river runoff water volume before it is sent to the coupler, compensating for what would be remapped by the coupler onto land points of the target grid and therefore lost in the masking. This approach guarantees that the volume of water going into the ocean matches the real runoff amount diagnosed in the atmosphere-land component.

The land frozen mass discharge scheme (discussed further in Section 3.2) in ACCESS-CM2 allows the snow/ice over Greenland and Antarctica to continuously accumulate. This is in contrast to ACCESS1.3 which placed a cap on land snow accumulation and dumped excess land snow into river run off. A free accumulation of land snow would lead to continual water loss from the global ocean, and therefore the land frozen mass discharge scheme provides the compensatory water flux to the ocean. However, the corresponding loss of water from the permanent ice regions is not applied in CABLE, and consequently due caution is required when analysing the water balance of these regions.

2.3 Ocean: MOM5

ACCESS-CM2 implemented the 2012 release of MOM model version 5 as the ocean component. Readers are referred to Griffies (2014) for a detailed description of the model fundamentals such as equations, physics and dynamics, supported coordinates, and sub-grid scale parameterisations. ACCESS-CM2 shares the same community numerical code as MOM5.1 (https://mom-ocean.github.io; hereafter MOM5 for simplicity) with a recently developed ocean-sea ice coupled model ACCESS-OM2 (Kiss *et al.* 2020), which is an enhanced version of ACCESS-OM (Bi *et al.* 2013*a*) with configurations for different resolutions.

MOM5 in ACCESS-CM2 for CMIP6 uses the same grid and resolution as that of MOM4p1 in ACCESS1.3 for CMIP5, as described by Bi *et al.* (2013*a*, 2013*b*). In brief, horizontally the ocean model has 360 longitude by 300 latitude points on a logically rectangular matrix, and vertically the z* coordinate is implemented, with 50 model levels covering 0–6000 m with a resolution ranging from 10 m in the upper layers (0–200 m) to about 333 m for the abyssal ocean. The horizontal discretisation is on an orthogonal curvilinear grid nominally 1 degree for both longitude and latitude, with refinements applied in three regions: (1) north of 65°N uses a tripolar grid (Murray 1996); (2) south of 30°S is smoothed with aspect ratio (dy/dx, varying between 1 and 1.4), which results in a latitudinal spacing ranging from 0.25° at 78°S to 1° at 30°S; and (3) the latitudinal spacing is refined to 1/3° between 10°S and 10°N. A similar smoothing with aspect ratio is also applied in the northern hemisphere (NH) between 30°N and 65°N. The vertical discretisation employs the z* coordinate of Adcroft and Campin (2004) and allows for partial grid cells at the base of the water column.

The ACCESS-CM2 implementation of MOM5 follows the MOM4p1 configuration for ACCESS1.3, but there are a few notable differences, as detailed below.

In ACCESS-CM2, shortwave penetration into the ocean is handled by the simplified CSIRO algorithm (as used for ACCESS1.3) and a more sophisticated GFDL scheme at different stages of the spin-up period (see Table 1). When the CSIRO scheme is used in the early stage of the spin-up, the maximum

penetration depth is set to the bottom of the ocean for ACCESS-CM2, compared with the 120 m limitation set in ACCESS1.3. The associated climatological shortwave attenuation depth (*SWAD*) data for ACCESS-CM2 has been switched to the diffuse attenuation coefficient (K_d, $SWAD = 1/K_d$) of the downwelling photosynthetically available radiation (K_{dPAR}) from the Sea-viewing Wide Field-of-view Sensor (SeaWiFS) Project dataset (Cracknell *et al.* 2001). In contrast, ACCESS1.3 inadvertently used K_{d490} (the default for the CSIRO SW scheme), which is the diffuse attenuation coefficient of the downwelling spectral irradiance at wavelength 490 nm, for the CMIP5 experiments (Dix *et al.* 2013; Marsland *et al.* 2013). The K_{dPAR} data covers a broader, more representative spectrum of light and is considered more appropriate for use in ocean models. Detailed discussions on the impact of shortwave attenuation depth datasets on ocean climate simulation were given in Bi *et al.* (2013*a*) and Zhou *et al.* (2015).

For the neutral physics parameterisation, both ACCESS-CM2 and ACCESS1.3 use isoneutral diffusion (Redi 1982) and a modified Gent and McWilliams (GM: 1990) scheme in which skew diffusion relaxes neutral directions towards surfaces of constant geopotential (Ferrari *et al.* 2010), with baroclinic closure of the thickness diffusivity. As the result of a series of mixed-layer depth tuning efforts, ACCESS-CM2 sets a GM eddy-induced advection diffusivity range of $100 \sim 1200\,m^2\,s^{-1}$, in contrast to that of $\sim$50–600 $m^2\,s^{-1}$ for ACCESS1.3. In addition, although both models set the constant Gent-McWilliams skew-diffusion diffusivity $agm = 600\,m^2\,s^{-1}$, ACCESS-CM2 and ACCESS1.3 set $aredi = 300$ and $600\,m^2\,s^{-1}$, respectively, for the constant neutral diffusion tracer diffusivity.

With regard to the eddy-induced friction, ACCESS-CM2 uses the same scheme as in ACCESS1.3 and ACCESS-OM which is described in Bi *et al.* (2013*a*). Horizontally, it is a combination of an isotropic Laplacian friction operator and a biharmonic friction operator, aimed to suppress grid noise inherent in under-dissipated flow simulations while allowing for strong boundary and equatorial current structures consistent with the model's grid resolution. The Laplacian viscosity is set by a constant velocity scale of $0.1\,m\,s^{-1}$ and the squared horizontal grid-scale. This viscosity is additionally scaled down in regions such as the tropics where the local Rossby radius of deformation is larger than the horizontal grid scale. The (Smagorinsky) biharmonic friction follows Griffies and Hallberg (2000) and its viscosity is enhanced in western boundary regions, with the Smagorinsky scaling coefficient for isotropic viscosity set to 2.0. Vertically, a background vertical viscosity of $1 \times 10^{-4}\,m^2\,s^{-1}$ is used, which is much enhanced in the mixed layer and thermocline following the K-profile parameterisation (KPP; Large *et al.* 1994), and an internal tidal mixing scheme (Simmons *et al.* 2004), which is most active in regions of pronounced bottom topography.

For the vertical mixing parameterisation, MOM5 and MOM4p1 both include three components: (1) KPP for the surface mixed layer; (2) a tidal mixing parameterisation for the abyssal ocean (Simmons *et al.* 2004) and coastal oceans (Lee *et al.* 2006); and (3) a background diffusivity (k_0) which is constant and globally uniform except in the tropical band ($|\varphi| \leq 20°$) where it is set to be latitude dependant – smoothly reduced from the nominal value at the north/south boundaries (k_0) to a minimum at the equator ($k_{eq} = 0.1 \times 10^{-5}\,m^2\,s^{-1}$). This approach is based on theory and observations that there are latitudinal bands with distinctly different diffusivities (see Jochum (2009) and references therein). However, there are two differences between the ACCESS-CM2 and ACCESS1.3 configurations. Firstly, the nominal value of background diffusivity k_0 is set to be 1×10^{-5} $m^2\,s^{-1}$ in ACCESS-CM2, consistent with that used for ACCESS-OM (Bi *et al.* 2013*a*) which is twice as large as that for ACCESS1.3. Secondly, the KPP mixing in ACCESS-CM2 is also strengthened by a new parameterisation of Langmuir mixing in KPP (Li *et al.* 2017) that applies an enhancement factor to the turbulent velocity scales. The direct effect of including Langmuir mixing in KPP is the deepening of the mixed layer depth through enhanced surface ocean mixing, and hence, we may expect some plausible impact on model climate in long-term simulations, especially in the Southern Ocean.

2.4 Sea ice: CICE5

The sea ice model CICE version 5.1.2 (Hunke *et al.* 2015; hereafter CICE5 for simplicity) is used as the sea ice component of ACCESS-CM2. CICE5 has been modified in ACCESS-CM2 for coupling to the atmosphere (UM) and ocean (MOM5) components. It is physically configured in the same manner as the Met Office Global Sea Ice model (GSI8.1; Ridley *et al.* 2018) which is the sea ice component of the Met Office HadGEM-GC3.1 (GC3.1 hereafter for simplicity) model. CICE5 uses an elastic-viscous-plastic dynamical scheme (Hunke and Dukowicz 1997) for the internal ice stress, and an incremental linear remapping for the ice advection term. The model has an ice thickness distribution which divides the ice into categories which evolve throughout the simulation due to thermodynamic growth and melt, and mechanical redistribution/ridging of the ice.

CICE5 in ACCESS-CM2 is horizontally configured on the ocean grid described earlier, which gives enhanced resolution in the Arctic due to the orthogonal curvilinear tripolar grid and in the Antarctic due to the Mercator grid with meridians converging at the South Pole (Bi and Marsland 2010; Uotila *et al.* 2012). The ice thickness distribution is represented by five ice thickness categories and an open water ice free area. In the vertical, the ice has four layers and a single snow layer on the surface when it is present. The ice and snow in each thickness category have their own vertical temperature profile and there is a prescribed vertical salinity profile, as salinity is not an active variable in this CICE5 set up.

The key differences between the CICE4.1 implementation for ACCESS1.3 and the CICE5 configuration for ACCESS-CM2 are the replacement of zero-layer thermodynamics with a multi-layer scheme as described in West *et al.* (2016), the addition of prognostic melt ponds, and the coupling to the atmosphere on ice thickness categories.

The CICE5 multilayer scheme allows the sea ice to have a temperature- and salinity-dependent heat capacity and hence conduction within the ice can vary in the vertical. The multilayer thermodynamics is based on that of Bitz and Lipscomb (1999) in which the diffusion equation with temperature-dependent coefficients is solved by the iteration of a tridiagonal matrix equation. For UM-CICE coupling purposes, this standard scheme has been modified (West *et al.* 2016), with surface exchange calculations carried out separately for each thickness category using JULES

within the UM code. This allows the near surface temperature to evolve smoothly on the atmosphere model time step, which is shorter than the coupling time interval. Previously, in the zero-layer sea ice case as in ACCESS1.3 and HadGEM3(r1.1), the UM calculated the diffusive heat flux all the way through the sea ice. Now the multilayer thermodynamics allows the CICE model to evolve a temperature profile, with all calculations performed within the sea ice model, while JULES calculates the surface exchange and the diffusive heat flux (for each ice thickness category) into the top ice layer only.

As in GSI8.1 for GC3.1, the CICE5 configuration for ACCESS-CM2 requires the ice-atmosphere coupling to pass additional fields for individual ice thickness categories. The fields required to be calculated for each thickness category are the thermodynamic fluxes (conduction, surface melt, sublimation), as well as snow depth and melt pond fraction and depth. Also, to calculate the surface exchanges, JULES requires extra coupling fields from CICE (see the next sub-section on the coupler and coupling strategy) as the lower boundary condition. The melt pond area fraction and depth on ice thickness categories are calculated with the CICE topographic melt pond formulation (Flocco *et al.* 2010, 2012).

CICE5 uses an albedo scheme based on that described in Hunke *et al.* (2015). It has separate albedos for visible and near-infrared wavelengths for both bare ice and snow. This new configuration used by ACCESS-CM2 includes the impact of surface melt ponds on albedo explicitly. The scheme calculates the total grid-box albedo of ice on ice thickness categories for each of the two wavebands by combining the albedo of the ponded fraction with the albedos of bare ice and snow, weighted by the melt pond fraction and snow fraction. Readers are referred to Ridley *et al.* (2018) for a detailed description.

2.5 Coupler and coupling strategy

ACCESS-CM2 uses the CERFACS OASIS3-MCT coupler (Valcke *et al.* 2015; Craig *et al.* 2017) to handle the inter-model communication and synchronisation. After compilation, the OASIS3-MCT coupling library is linked to the component models of the coupled system; its main function is to interpolate and exchange the coupling fields as required. At run time, all transformations are performed in parallel on the set of source or target component processes, and all coupling exchanges are now executed in parallel directly between the component processes via the Message Passing Interface (MPI). Therefore, unlike OASIS3.2–5 (Valcke 2006) as used in ACCESS1.3, the OASIS3-MCT coupler is not a standalone component, and the coupling executions between sub-models are significantly more scalable and efficient.

Despite this change, however, the coupling approach in ACCESS-CM2 remains the same as that described in ACCESS-OM (Bi *et al.* 2013*a*) and ACCESS1.3 (Bi *et al.* 2013*b*). Other than necessary modifications to the coupling code to reflect the MCT parallel coupling, use of OASIS3-MCT does not change the structure of the existing coupling interfaces in CICE and MOM written based on OASIS3.2–5, and the coupling configuration file remains largely the same but with the addition of more coupling fields. As mentioned earlier, ACCESS-CM2 has implemented the multilayer sea ice thermodynamics and added prognostic melt ponds in CICE5. This change results in a large increase in the number of coupling fields exchanged between the atmosphere and sea ice. See Table A1 for a list of the ACCESS-CM2 coupling fields involved in the atmosphere-sea ice and sea ice-ocean communications, which includes the full subset of the coupling fields used for ACCESS1.3. Also included in Appendix A1 are details of some new variables and the coupling strategy.

3 Experimental design

The experimental framework for an entry-level CMIP6 submission involves initialisation, a multi-century spin-up run under the CMIP6 PI forcing conditions, followed by the four official CMIP6 DECK experiments (Eyring *et al.* 2016) comprising PI control (hereafter *piControl*), a 1% per year CO_2 increase run (*1pctCO2*), an abrupt $4 \times CO_2$ run (*abrupt4xCO2*), an Atmospheric Model Intercomparison Project simulation with prescribed sea surface temperatures (*amip*), and a *historical* simulation over the period 1850–2014. This paper only documents the spin-up procedure and evolution of the model climate during the 950-year spin-up integration.

3.1 Initialisation and forcing set up

Initialisation of the ACCESS-CM2 PI spin-up includes three parts: (1) initialising the atmospheric and land surface using the state of 1 January 1979 obtained from an atmosphere (UM)/land (JULES) model simulation; (2) initialising the ocean state using the ocean climatological temperature and salinity fields for January from the World Ocean Atlas 2005 (WOA2005) (Antonov *et al.* 2006; Locarnini *et al.* 2006). We note that this a deviation from the Ocean Model Intercomparison Project (OMIP; Griffies *et al.* 2016) protocol for CMIP6 that uses WOA13v2 (Boyer *et al.* 2015). The ocean is set with no motion at the beginning, allowing the model physics to spin up a velocity field in balance with the density structure of the water; (3) initialising the sea ice state using the WOA2005 January sea surface temperature (SST) and salinity (SSS). Any grid point that has SST equal to or lower than the SSS-dependent freezing point is set to have 5-thickness-category ice areas which together fully cover the cell. The 5 ice thickness categories are initialised with values in the middle of their designated ranges and the overall distribution is weighted to give a mean thickness of 3 m in the Arctic and 1 m in the Antarctic. The initial temperature profile in the ice is linear between the temperature at the snow surface (which will come from the atmosphere model initial condition) and the freezing temperature at the ice base. Snow cover over the ice is set to be 0.20 m thick initially, but it will either melt or accumulate in response to the climatological forcing from the atmospheric model and settles into a seasonal cycle.

The atmospheric forcing for the ACCESS-CM2 PI spin-up and *piControl* simulation follows Eyring *et al.* (2016) and includes the standard CMIP6 PI (i.e. around 1850) prescription of the major greenhouse gases (i.e. CO_2, CH_4, N_2O), ozone, the solar constant, aerosol related emissions of SO_2, BC and OC, and a background volcanic aerosol forcing in the stratosphere. Throughout the ACCESS-CM2 PI spin-up and *piControl* run, the solar constant is set to be 1361 W m^{-2}; the concentrations of

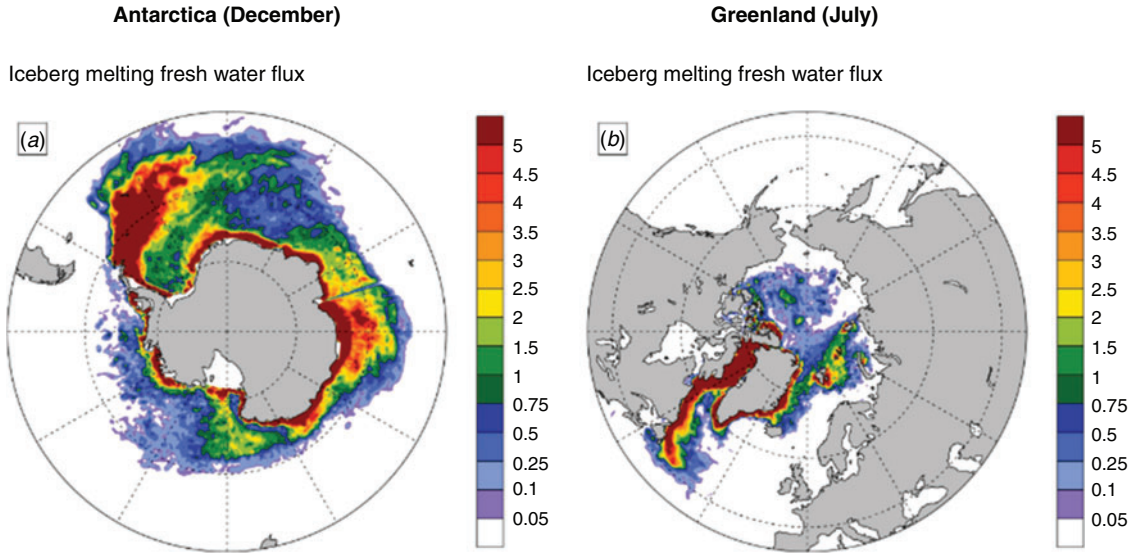

Fig. 1. Summer distributions of the ACCESS-CM2 land ice discharge into ocean (as iceberg melting) water fluxes around: (*a*) Antarctica (December), and (*b*) Greenland (July). Units: mm day^{-1}.

the major atmospheric greenhouse gases are prescribed to be: $CO_2 = 284.317$ ppmv, $CH_4 = 808.25$ ppbv, and $N_2O = 273.02$ ppbv; and the seasonally-varying biogenic aerosol emissions and a background volcanic SO_2 out-gassing flux (into the lower to mid troposphere) are maintained.

3.2 Land frozen mass discharge scheme

We discharge the accumulated "snow amount on land ice" ("land ice" for simplicity) over Greenland and Antarctica as iceberg calving into the ocean to balance the oceanic water mass loss. Such discharge in ACCESS-CM2j was initially conducted for every atmosphere-sea ice coupling interval (i.e. instantaneous), but it has eventually been changed to a constant model climatology forcing (i.e. monthly water and heat fluxes, see below) to the ocean. This helps maintain the water mass balance of the global ocean and constrains the warm bias in the Southern Ocean for long equilibrium simulations, while also avoiding contaminating the climate change signal (because of instantaneous "correction" to water mass loss from ocean) under external forcing scenarios.

The model climatology forcing of iceberg melting is obtained from an early multi-century PI spin-up run using ACCESS-CM2j. Put simply, the NH and the southern hemisphere (SH) land ice increments are diagnosed for each coupling interval in the ice model (and discharged into the ocean) in the ACCESS-CM2j spin-up run, and the data for the first century (years 2–101) is used to get the monthly climatology of the land ice discharge. Then we distribute this climatology of NH and SH land ice amounts onto the distributional map of the iceberg climatology from the GC3.1 Lagrangian iceberg model (D. Storkey, pers. comm.). The ACCESS-CM2 climatology of monthly iceberg flux is then the product of the GC3.1 climatology of iceberg flux multiplied by the ratio of annual total land ice discharge of ACCESS-CM2j to the annual total iceberg amount of GC3.1. Fig. 1*a* and *b* show the summer distribution of the ACCESS-CM2 iceberg melting water fluxes in the SH (December) and NH (July) ocean, respectively, representing the largest iceberg fluxes of the annual cycle.

The resulting ACCESS-CM2j iceberg flux climatology is then read in by the ice model and passed into the ocean model via the OASIS3-MCT coupler as a monthly mean forcing, replacing the discharge obtained from the diagnosed land ice increment at each UM-CICE coupling interval. Also passed into the ocean is the accompanying heat flux that is simply assumed to be required for melting the ice at the local SST. Such heat fluxes (f_{heat}) are proportioned to the freshwater flux (f_{water}), namely, $f_{heat} = -L_{fw} \times f_{water}$, where $L_{fw} = 3.34 \times 10^5$ J kg^{-1} is the latent heat of melting of fresh ice. Here, f_{heat} and f_{water} improve the model simulation by cooling and freshening the surface layer water off Greenland and Antarctica. We have spun-up ACCESS-CM2j with this iceberg discharge for a multi-centennial period and found significant improvement of the sea ice simulation in the Southern Ocean where the sea ice would otherwise disappear nearly completely during the Austral summer without such additional fresh water and heat fluxes from the land ice.

This land ice discharge (as iceberg melting) provides a global averaged annual mean freshwater flux of 2.054×10^{-7} kg m^2 s^{-1} (0.01775 mm day^{-1}) into the ocean, of which about 79% comes from Antarctica. The associated global average heat flux into the ocean is –0.0686 W m^{-2}. The replacement of JULES with CABLE for land surface representation changes snow accumulation, and scaling factors for the land ice discharge are derived accordingly. The ACCESS-CM2j iceberg flux is used with an enhancement factor of 1.16 and 1.65 applied to the discharge from Antarctica and Greenland, respectively, which maintains a close balance of the global ocean water mass in the CABLE version ACCESS-CM2 spin-up, as shown below.

We note that such specific land ice discharge is not needed in ACCESS1.3 due to its cap for land snow accumulation. As shown later, ACCESS1.3 still has better simulation of SST and sea ice off Antarctica than ACCESS-CM2. This difference is attributed to

the updated radiation and more complex aerosol schemes in the UM GA7.1 atmospheric configuration (for ACCESS-CM2 and GC3.1), which result in large warm biases in the SH and cold biases in the NH. The land-ice mass discharge scheme described here does not solve this problem but reduces the (warm) biases around Antarctica.

3.3 Spin-up procedure

Here we document the ACCESS-CM2 spin-up procedure, including some of the debugging and tuning efforts over the course of model development. The initial spin-up was conducted with ACCESS-CM2j for several centuries and the official version of ACCESS-CM2 took over during the sequence of simulations when CABLE was successfully implemented into the system. Table 1 provides a "chronological" chain of the consecutive runs comprising the spin-up simulation, involving work with firstly JULES, then CABLE versions, providing traceability of the ACCESS-CM2 CMIP6 experiments.

As shown in Table 1, the PI spin-up simulations for ACCESS-CM2j and ACCESS-CM2 were continued for a total of 950 years, significantly longer than that for the ACCESS CMIP5 models (300 years for ACCESS1.0 and 250 years for ACCESS1.3). Although they have been subject to moderate perturbations because of tuning and debugging in the course of progress, especially for the CABLE version whose final integration with "frozen" configurations is relatively short, we judge the ocean interior has evolved adequately toward a quasi-equilibrium[1] and is appropriate for commencing the CMIP6 experiments (e.g. *piControl*, *historical* simulations).

4 Preindustrial spin-up results

In this section, we provide basic evaluation of the ACCESS-CM2 and CM2j PI spin-up simulations. We choose to present a selection of key fields in terms of temporal evolutions for the 500-year period starting from year 450 and ending at year 949. Also presented are the results of the ACCESS1.3 500-year *piControl* run, which was the continuation of ACCESS1.3 spin-up from year 250 (Bi *et al.* 2013*b*). A "spin-up climatology" is also defined as the time average over the last century of the 500-year period selected, namely, years 850–949 for ACCESS-CM2 and CM2j, and years 650–749 for ACCESS1.3. For ease of comparison for temporal evolutions, we redesignate the first year of the 500-year periods as year "1". Because of the close similarity of the ACCESS-CM2 and CM2j results, we choose to omit the CM2j results when comparing the spin-up climatology of the two-generation models other than where it is needed. In addition, because of the lack of observations for the PI climate, recent observations are used where applicable for assessing the PI spin-up results of the models on the basis that the models' PI run (to be shown here) and present-day control simulations (with year 2000 atmospheric condition, performed earlier and not shown here) are quite similar in terms of fundamental features for the chosen subset of variables discussed below.

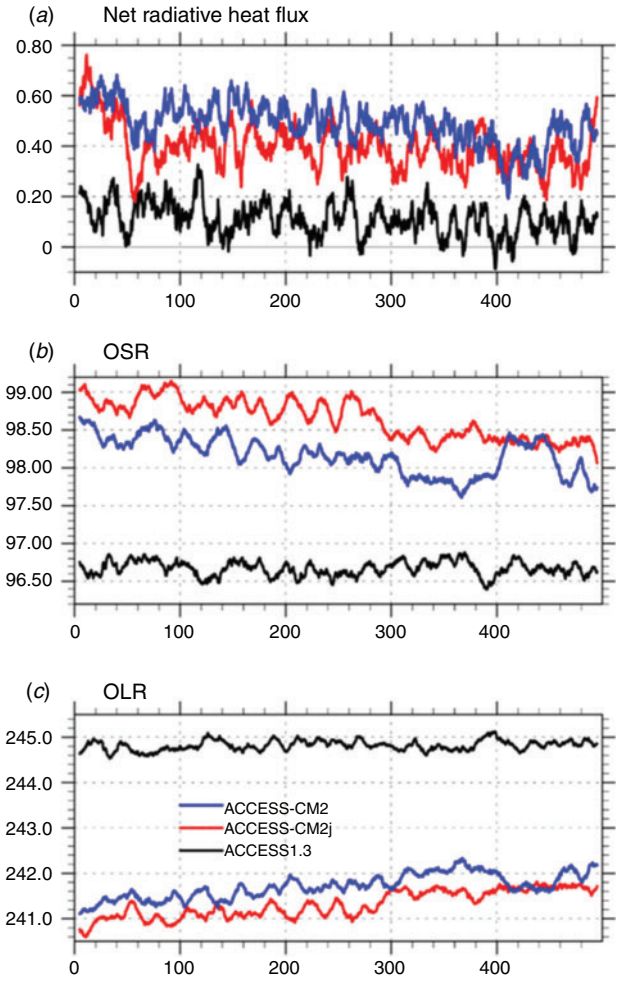

Fig. 2. Evolution of global mean radiations at the TOA: (*a*) net radiation (positive inwards), (*b*) outgoing shortwave radiation (OSR, positive outwards), and (*c*) outgoing longwave radiation (OLR, positive outwards). A 10-year running mean is applied to all variables. Units: W m^{-2}.

4.1 Radiation budgets at the top of atmosphere

Fig. 2*a* shows the evolution of the global net radiation (positive downward) at the top of atmosphere (TOA) in the selected 500-year PI simulation period of the three models. The ACCESS-CM2 models gradually stabilise at around a level of 0.35 W m^{-2} (with CM2j being slightly less than CM2), similar to the ACCESS1.0 result (Bi *et al.* 2013*b*) but significantly larger than ACCESS1.3's long-stabilised level of imbalance of <0.1 W m^{-2} that is well within the criteria for long *piControl*/spin-up runs (e.g. Gent *et al.* 2011). The energy imbalance at TOA in the ACCESS-CM2 models implies continuous heat uptake of the earth system and we will see later that the ocean internal temperature increases nearly linearly.

Fig. 2*b, c* shows the time series of the TOA outgoing shortwave and longwave radiations (OSR and OLR) respectively, for the

[1]Ideally the deep ocean should be spun up until reaching equilibrium, but it would require thousands of years integration (e.g. Stouffer 2004) and is practically unaffordable.

Table 2. The last 100-year mean of the TOA global mean radiation budget, outgoing shortwave and longwave radiations (OSR, OLR), planetary albedo, and their hemispheric gradient (northern – southern: N-S) of the ACCESS models. Also listed in the table are the observations (e.g. Allan *et al.* 2014; Stephens *et al.* 2016) for present-day climatology and result (years 400–500 mean) from a GC3.1 run (Kuhlbrodt *et al.* 2018) that was performed with the N96ORCA1 version (N96 UM and 1-deg ocean) under constant present-day forcing (i.e. year 2000 condition of CO_2 and aerosols). GM = global mean; net radiation is positive down while OSR and OLR are positive up; the observed net radiation budget is from Allan *et al.* (2014) for the period of 2000–2012. Note the GC3.1 result and observations are presented here for general reference, not for the purpose of calibrating and validating the PI simulations of the ACCESS models because of the different PI and present-day atmospheric conditions (greenhouse gases and aerosols)

	Net radiation budget ($W m^{-2}$)		OSR ($W m^{-2}$)		OLR ($W m^{-2}$)		Albedo (none)	
	GM	N–S	GM	N–S	GM	N–S	GM	N–S
ACCESS1.3	0.04	–2.26	96.67	–2.48	244.8	4.93	0.2829	–0.004
ACCESS-CM2j	0.32	–4.35	98.54	1.86	241.4	2.67	0.2895	0.008
ACCESS-CM2	0.37	–4.96	97.99	1.58	241.9	3.56	0.2879	0.007
HadGEM-GC3.1	0.35	–4.60	99.30	2.35	240.7	2.70	0.2920	0.009
Observations	0.62 ± 0.43	–1.20	$99.65 \pm 2 \sim 3$	–0.1	$239.6 \pm 2 \sim 3$	1.30	0.2930	–

three runs. Both the OSR and OLR in ACCESS1.3 have settled at equilibrium over the whole period but in ACCESS-CM2 and CM2j they have not yet stabilised, and the apparent net radiation quasi-equilibrium of these two models in the last 200 years shown in Fig. 2*a* actually results from a near cancelation of the opposite trends in global mean OSR (decreasing) and OLR (increasing). Moreover, ACCESS-CM2 and CM2j simulate evidently smaller OLR but larger OSR than ACCESS1.3 at TOA.

Table 2 shows that all models correctly give negative NH to SH gradient (N-S gradient for simplicity) of the TOA net radiation, indicating the system loses energy in the NH and gains energy in the SH. ACCESS1.3 has a N-S gradient of net radiation of $-2.26\ W m^{-2}$, roughly half of that seen in the ACCESS-CM2 models. This relatively small gradient results from the abnormally large gradients of OLR (positive) and OSR (negative) cancelling each other, which is not the case for the ACCESS-CM2 models (and is not seen in the present-day observations and the GC3.1 simulation (Kuhlbrodt *et al.* 2018)). It is hard to judge the realism of these ACCESS simulations in this aspect due to lack of PI observations, but we can see the difficulty of realistically representing such radiative condition at the TOA. For example, the GC3.1 present-day simulation gives a global mean N–S gradient of $-4.60\ W m^{-2}$, which is somehow close to the ACCESS-CM2 PI results but nearly 4 times the estimate from present-day observations. This large deviation of the GC3.1 simulation from the observations is the joint result of the modelled large N–S gradients of OSR and OLR, but it is the strong reflectivity in the NH that makes the most contribution, as evidenced by the contrast of OSR N-S gradient between the model ($2.35\ W m^{-2}$) and the observations ($-0.1\ W m^{-2}$).

That the GC3.1 model shows too strong a reflectivity in the NH indicates the model's deficiency in handling atmospheric processes such as cloud, aerosol and solar radiation. This deficiency in atmosphere is carried on to the ACCESS-CM2 models which share the same UM model and atmospheric configuration with GC3.1, and we see similar results in the PI simulations presented here, despite the different conditions of greenhouse gases and aerosols. For ACCESS1.3, the missing dust load in the atmosphere (as noted in Section 2.1) is estimated to reduce the global mean OSR by $<0.5\ W m^{-2}$, therefore adding the dust effect would slightly increase the ACCESS1.3 OSR (from 96.67 to $<97.17\ W m^{-2}$), and, if we assume it all goes into the NH, it would change the OSR N–S gradient from –2.48 to at most $-1.48\ W m^{-2}$, still in contrast to the ACCESS-CM2 models which shows notably stronger reflectivity in the NH than in the SH.

Under the PI forcing condition, ACCESS1.3 shows the smallest planetary albedo (0.2829) and ACCESS-CM2j produces the largest (0.2895). The ACCESS-CM2 result being slightly smaller than that of ACCESS-CM2j is at least partly attributed to the ocean albedo adjustment – as stated in Table 1, the 2% enhancement of ocean surface albedo (which has been applied throughout the ACCESS-CM2j run) has been removed in the last 100-year period of the ACCESS-CM2 spin-up. All the ACCESS results from PI spin-ups are smaller than that from the GC3.1 present-day simulation and observations but may not be deemed as unreasonable for the individual models because of the sophisticated dependence of the earth's planetary albedo on cloud amount and properties, radiative effects of greenhouse gases and aerosols, land use and ice/snow coverage on the earth surface.

4.2 Global precipitation

Fig. 3 presents the Global Precipitation Climatology Project (GPCP) 1979–2016 observations annual mean precipitation (Adler *et al.* 2018) and biases of the ACCESS1.3 and ACCESS-CM2 PI spin-up climatology relative to the GPCP data. The two models show very similar global distributions of the annual mean precipitation and both have noticeable errors (Fig. 3*b, c*), particularly over the tropical regions. The common issue of a double intertropical convergence zone (ITCZ) in the Pacific Ocean is evidenced by the excessive rainfall south of the equator and reduction to the north of the equator, and this error is more pronounced in ACCESS-CM2 as shown in Fig. 3*b, c*. The meridional wave-like pattern of the biases in the tropical oceans arises from a misrepresentation of the ITCZ and its seasonal cycle, and it is resolution-independent in the UM (Kuhlbrodt *et al.* 2018). In the equatorial Atlantic Ocean, the positive rainfall bias

found in ACCESS1.3 also becomes larger in ACCESS-CM2. However, the excessive rainfall simulated by ACCESS1.3 in the tropical Indian Ocean, with the maximum error being five times that in the observations, has been substantially reduced in ACCESS-CM2. Similar improvement in ACCESS-CM2 can also be found over the maritime continent.

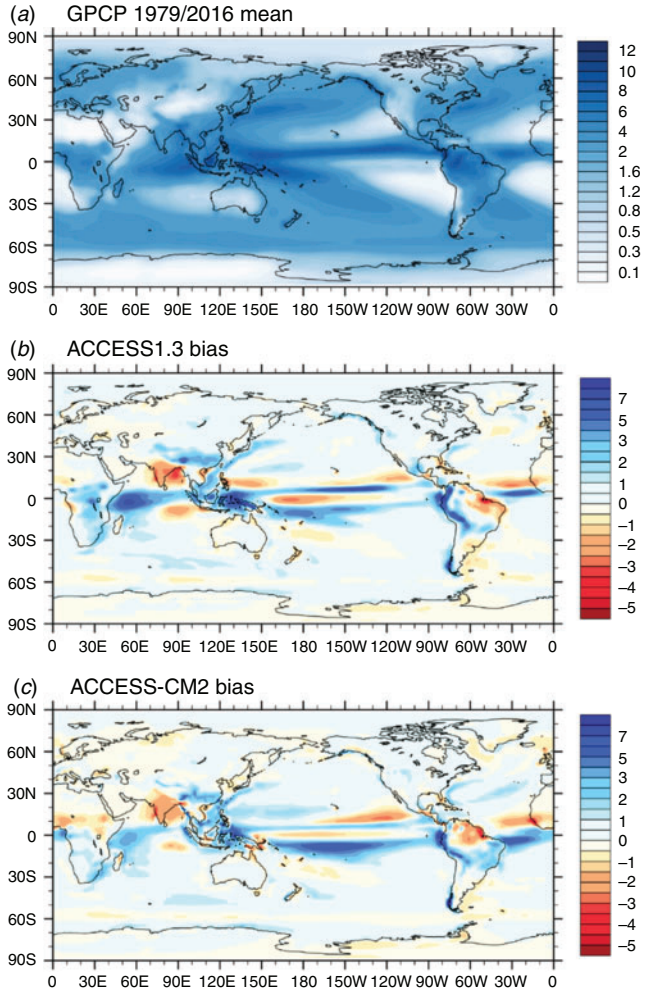

Fig. 3. Precipitation observations and model biases: (*a*) GPCP data 1979–2016 mean; (*b*) ACCESS1.3 biases; (*c*) ACCESS-CM2 biases. Note the uneven contour intervals for different ranges in (*a*): 0.1 for 0 ~ 0.6, 0.2 for 0.6 ~ 2, and 1 for the band beyond 2. Units: mm day^{-1}.

Globally, both models simulate more rainfall than the present-day observations, with ACCESS-CM2 being slightly better than ACCESS1.3, as indicated by the model biases and the "error ratios" (ER, i.e. error-to-observation ratios) given in Table 3. Kuhlbrodt *et al.* (2018) pointed out that the excess global mean precipitation is a long-standing issue with the UM and other global atmospheric models (Collins *et al.* 2010). The ACCESS models' precipitation rates under PI condition (3.178 mm day^{-1} for ACCESS1.3 and 3.126 mm day^{-1} for ACCESS-CM2) are slightly higher than that from the GC3.1 present-day simulations (e.g. 3.07 mm day^{-1} for the GC3.1 N96 version).

Over the ocean, the two ACCESS models have similar performance. The large root-mean-square-errors (RMSEs) are mostly attributed to the large errors in the tropical regions shown in Fig. 3*b* and *c*. The models also perform poorly along the west coast of the South American continents (the ocean upwelling region) where the largest error-to-observation ratios are located. In fact, this upwelling area and its extension in the sub-tropical Pacific Ocean have the most noticeable positive error ratio for both models (data not shown), which is associated with the models' spuriously large surface warm biases over the region (to be shown in Section 4.3) and the observations showing very little precipitation (Fig. 3*a*). The large positive error in the western tropical Indian Ocean seen in ACCESS1.3 is considerably reduced in ACCESS-CM2. In addition, it may be worth mentioning that both models, especially ACCESS-CM2, simulate slightly less precipitation than observed along the Antarctic Circumpolar Current (ACC).

Over the land, ACCESS-CM2 seems to perform better than over the ocean in terms of both the simulated magnitude and distribution of precipitation. Particularly, the error ratio (7%) is less than half of that over the ocean (18%). Note this error rate is only one-third of its counterpart (21%) in ACCESS1.3, which is even larger than that over the ocean (17%). Both models show noticeable negative errors over India and northern South America, and positive errors over China and central South America. However, ACCESS-CM2 shows more moderate rainfall errors over the African continent and does not produce the noticeable positive errors in tropical Africa seen in ACCESS1.3 (Fig. 3*b*). Over Australia, both models simulate precipitation quite close to the observations everywhere except Western Australia where ACCESS1.3 shows slight negative errors and Cape York (and north) where ACCESS-CM2 simulates noticeably less rainfall.

Table 3. GPCP present-day (1979–2016) observed precipitation (Adler *et al.* 2018), ACCESS-CM2 and ACCESS1.3 PI spin-up biases, error ratios (bias/observation, %), and RMSEs. Also included is the precipitation difference between the two models (ACCESS-CM2 minus ACCESS1.3). Except the error ratios (ERs), all items have units of mm day^{-1}

	GPCP	ACCESS1.3			ACCESS-CM2			ACCESS-CM2–ACCESS1.3
		Bias	ER (%)	RMSE	Bias	ER (%)	RMSE	
Global	2.690	0.488	18	1.376	0.436	16	1.285	–0.052
Land	2.009	0.426	21	1.309	0.143	7	1.023	–0.283
Ocean	2.919	0.508	17	1.398	0.534	18	1.362	0.026

4.3 Sea surface features

4.3.1 Sea surface temperature

Fig. 4*a* shows the evolution of global average annual mean sea surface temperature (SST). Compared with ACCESS1.3, where the temperature is relatively stable across the 500-year simulation, the ACCESS-CM2 models undergo evident warming in the first 300 years (i.e. model years 450–749) and then start stabilising. This difference is due to the "coupling shock" (abrupt cooling and freshening, not shown) that occurs at the beginning of the spin-up run that is much larger in ACCESS-CM2 than ACCESS1.3. In fact, ACCESS1.3 sees a global mean cooling of merely ~0.3°C in the first 10 years and then a rapid recovery over the next couple of decades. For ACCESS-CM2j; however, the global mean SST drops ~1°C in the first 25 years or so and stays at that level for many decades before starting a slow recovery. This recovery lasts for many hundreds of years until the global mean SST finally catches up with the level of ACCESS1.3 in the late stage of the spin-up, as shown in Fig. 3*a*. The reason for the remarkable difference in coupling shock and recovery between ACCESS1.3 and ACCESS-CM2j is unclear and requires further investigation. ACCESS-CM2 generally follows the track of ACCESS-CM2j but shows significant adjustment (dipping and recovery) in the last century due to changes made in the CABLE model configuration (see Table 1).

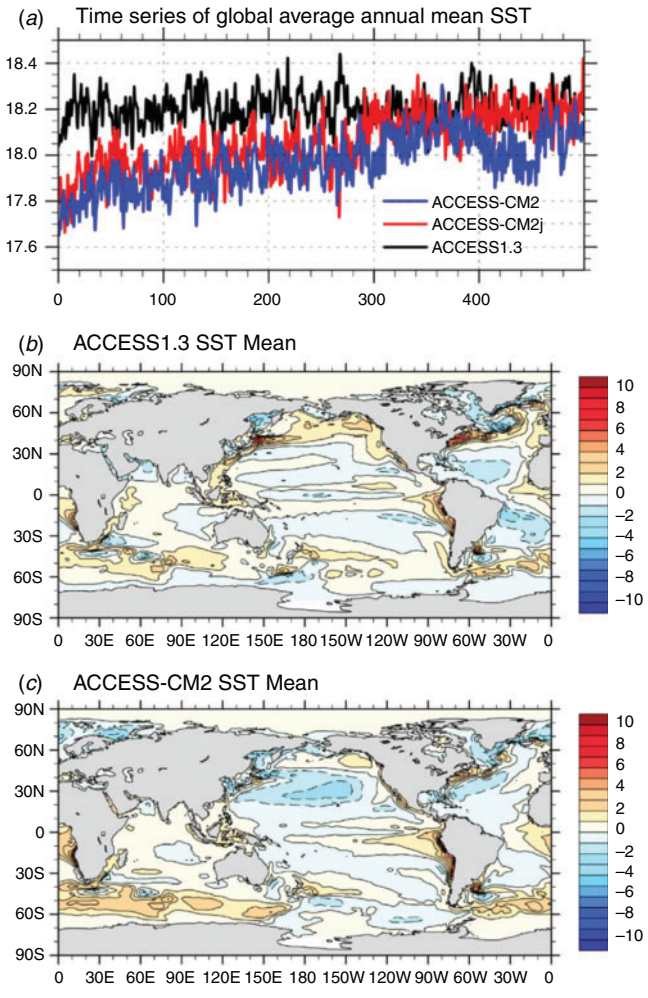

Fig. 4. (*a*) Time series of global average annual mean SST. (*b*) Annual mean SST biases of ACCESS1.3 (last 100-year average minus 1870–1900 SST reconstruction from HadISST (Rayner *et al.* 2003)). (*c*) Same as (*b*) but for ACCESS-CM2. Units: °C.

Fig. 4*b, c* present the global pattern of annual mean SST biases for ACCESS1.3 and ACCESS-CM2, respectively. ACCESS-CM2 has a global mean bias of 0.13°C, better than the 0.26°C error of ACCESS1.3, indicating an overall closer agreement of ACCESS-CM2 with the observations. However, in ACCESS-CM2 the standard deviation (RMSE) of 1.17°C is larger than that of ACCESS1.3 (1.06°C), meaning a poorer SST pattern in the new model, as evidenced by the two maps in Fig. 4. For example, compared with ACCESS1.3, ACCESS-CM2 has much larger areas of cold biases (in the North Pacific) and warm biases (in the Southern Ocean). Such "unbalanced" geographical distribution of warm and cold biases in ACCESS-CM2 is also found in the Met Office GC3.1 model (Kuhlbrodt *et al.* 2018). It is largely associated with the UM model configuration, especially the physical parameterisations such as the aerosols, clouds and radiation schemes, and aligns with the significant NH-SH asymmetry of the TOA net radiation budget found in ACCESS-CM2 and GC3.1 (Table 2). Differences in the SST biases in the Southern Ocean, especially the Antarctic coastal regions where ACCESS1.3 shows no warm bias or even a slight cold error while ACCESS-CM2 shows small warm errors, are of climatic significance. They result in considerably different performance in sea ice simulations of the two models, as presented in Section 4.4.

While ACCESS-CM2 and ACCESS1.3 show generally similar SST biases in the Indian Ocean and South Pacific, ACCESS-CM2 presents some noticeable improvements over ACCESS1.3 in a few regions. For example, the broad cold biases found over the 40°S–40°N band of the Atlantic Ocean in ACCESS1.3, which is mainly attributed to the error in SW cloud radiative forcing (Bi *et al.* 2013*b*), are not seen in ACCESS-CM2, indicating improvement of the cloud simulation there. In addition, the large warm biases shown in Fig. 4*b* along the major frontal zones such as the western boundary currents in the North Pacific (Kuroshio Current) and North Atlantic (Gulf Stream) are significantly reduced in Fig. 4*c*.

It is well known that a coarse (i.e. non-eddy permitting) resolution of the ocean model does not represent the frontal current structures and positions properly. Ocean frontal zones have strong horizontal gradients of temperature, therefore any errors of location and intensity of the modelled frontal flows (associated with the overlying atmospheric forcing) result in large local SST biases in these locations. The reason for the improvement of the ACCESS-CM2 simulation over these frontal zones is not clear and requires further investigation. In ACCESS1.3, the strong cold bias (up to 5–6°C) located southeast of the Labrador Sea, is a common issue of 1° resolution ocean models (Danabasoglu *et al.* 2014) due to their deficiency in representing the Gulf Stream path, which in reality turns east at higher latitudes so that the warm (and salty) waters from low latitudes are transported into the northern North Atlantic. This cold error is also significantly reduced (down to 2–3°C) in ACCESS-CM2.

One of the notable deficiencies, common to both ACCESS1.3 and ACCESS-CM2, is the tongue of warm biases off the west coasts of America and Africa. This is also a common error shared by many coarse resolution ocean models as shown by Griffies *et al.* (2009), caused by the model underestimating the coastal upwelling and associated westward mass transport. A test simulation using a prototype version of ACCESS-CM2, which was configured with N96 UM/GA6 atmosphere and $\frac{1}{4}^\circ$ MOM5 ocean, showed that these large west coast warm biases are substantially reduced, confirming the importance of higher resolution for representing the ocean dynamic processes, such as coastal upwelling.

We note that, for ACCESS1.3, the SW penetration misconfiguration mentioned in Section 2.3 may have to some extent intensified the warm biases in the west coastal regions off South America and South Africa in particular. As discussed in Bi *et al.* (2013*a*), such "additional" warming originates from the subsurface water which is warmed by the deeper short-wave penetration (associated with using of K_{d490}) and upwelled to the surface.

4.3.2 Sea surface salinity

Fig. 5*a* shows the evolution of annual mean global average sea surface salinity (SSS) of the three spin-up simulations. All models have generally stabilised, but the SSS equilibria of ACCESS1.3 and ACCESS-CM2/CM2j deviate from each other. This difference results from a much larger coupling shock in ACCESS-CM2, which brings the global mean SSS from the initial level of 34.72 psu down to 34.45 psu within the first hundred years (not shown), and the freshening continues throughout the course of the spin-up at a decreasing rate which results in a further SSS decrease of 0.08 psu in the last 850 years of the total 950-year spin-up. For ACCESS1.3, the coupling shock brings the global mean SSS down to 34.55 psu in the first 80 years, but after that the SSS starts a slow but steady recovery, which leads to a final global mean SSS of 34.65 psu, quite close to the initial condition. The SSS evolution of ACCESS-CM2 generally follows that of ACCESS-CM2j, but it is more stable across the simulation.

Fig. 5*b, c* present the maps of global average annual mean SSS biases (relative to present-day observation) of ACCESS1.3 and ACCESS-CM2, respectively. In the two maps, broad similarity is seen in the Arctic Ocean, Indian ocean, and South Atlantic whilst differences are evident in the other basins. Overall, the ACCESS-CM2 result is much fresher than that of ACCESS1.3 across the whole Pacific Ocean, most of the Atlantic Ocean and the Southern Ocean. In fact, the global mean SSS bias is –0.025 psu in ACCESS1.3 and –0.221 psu in ACCESS-CM2, with the RMSE being 1.303 psu and 1.743 psu for the two models, respectively, showing larger spatial deviation of ACCESS-CM2 from the observations. Like ACCESS1.3, ACCESS-CM2 sees large fresh biases in the East Asian marginal seas, North Sea, Baltic Sea and Gulf of Bothnia, and particularly Hudson Bay. As discussed in Bi *et al.* (2013*b*), these large fresh biases are associated with river routing errors in the land surface model and the inability of a coarse resolution ocean model to properly represent the circulation in marginal seas with limited connection to the open ocean.

Noticeable positive salinity biases are found in several places: large salinity errors occur in the Arctic Ocean (north of Siberia),

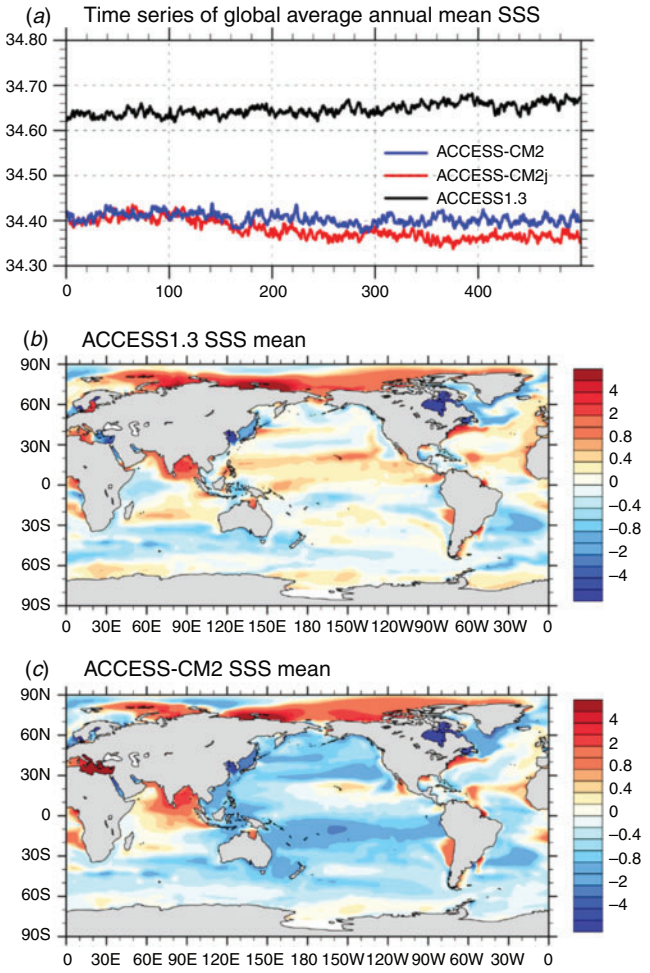

Fig. 5. (*a*) Time series of global average annual mean SSS. (*b*) Annual mean SSS biases of ACCESS1.3 (last 100-year average minus WOE2009 observation (Locarnini *et al.* 2010)). (*c*) Same as (*b*) but for ACCESS-CM2. Contour interval is 0.2 for range –1 ~ 1, and 1 for bands beyond this range in (*b*) and (*c*). Units: psu.

possibly resulting from poor representation of river runoff in the land model and observation errors in ice covered waters; a large region of high salinity biases in the Arabian Sea and the Bay of Bengal, which is associated with the negative rainfall bias there (as shown in Fig. 3). Also, ACCESS-CM2 produces a large salinity error over the whole Mediterranean Sea, whereas ACCESS1.3 sees fresh biases in the Eastern Mediterranean Sea. Such differences may be attributed to the different local rainfall biases in the models. Fig. 3*b, c* show that ACCESS-CM2 and ACCESS1.3 have mild negative and positive errors, respectively, in the Eastern Mediterranean Sea, which causes 0.4 mm day^{-1} less rainfall in ACCESS-CM2 than ACCESS1.3. A lack of efficient connectivity with the North Atlantic, due to the constriction of the Strait of Gibraltar, allows this salinity bias to increase over the course of the integration.

That the global ocean surface water is about 0.25 psu less saline in ACCESS-CM2 than in ACCESS1.3 (Fig. 5*a*) may be attributed to slightly more rainfall (0.026 mm day^{-1}, as shown in

Table 3) over the ACCESS-CM2 ocean, plus somewhat more runoff from land (not shown). Despite the large error of lower SSS, ACCESS-CM2 actually has a well-balanced sea surface water flux budget, which leads to a stable water volume for the ocean and constant global ocean salinity. In contrast, ACCESS1.3 undergoes a continuous increase of the global ocean salinity although it has a much smaller salinity error at the surface. This comparison is presented in Section 4.5.

4.4 Sea ice

Fig. 6*a, b* show the annual cycle climatology of sea ice extent for the NH and SH, respectively, from the model results (last 100-year mean) and the HadISST reconstructed ice concentration (Rayner *et al.* 2003) for the periods of 1947–1977 (which is just prior to the satellite era) and 1978–2019 (satellite era). The pre-satellite observational data is used to evaluate the models' ice simulation under PI condition over the NH, as Walsh *et al.* (2015) have reconstructed the ice extent from 1850 and shown no dramatic change of the NH sea ice coverage prior to the mid–1970s but unprecedented decrease from the late 1970s onwards. However, we choose the satellite-era data (1978–2019) to evaluate the models' ice simulation around Antarctica because of lack of enough reliable data records in the SH prior to the satellite era.

We see that the ACCESS-CM2 models yield nearly identical PI spin-up climate of the sea ice coverage year-round in both the NH and SH, and they noticeably deviate from the ACCESS1.3 result and the observational estimates. In the NH, compared with the pre-satellite observations, the ACCESS1.3 result is close to the present-day satellite observations and thus underestimates the Arctic sea ice extent in all seasons under PI condition, while the ACCESS-CM2 models gives a better annual mean ice coverage but noticeably overestimate the late-winter ice growth and summer ice retreat. The cause of the winter maximum sea ice extent in the ACCESS-CM2 models being considerably larger than ACCESS1.3 (and observations) is related to the models' winter air temperature being 3°C colder over the Arctic Ocean than ACCESS1.3, consistent with a (up to ~7 hPa) stronger high-pressure system over the Beaufort Sea (not shown). This very strong Beaufort system has existed since the UM GA6.0 and is associated with implementation of the ENDGame dynamical core (see Section 2). In the SH, however, the situation is reversed. The ACCESS-CM2 models show noticeable scarcity of ice around Antarctica at most times of the year (i.e. Jan–Oct.). Particularly, they largely overestimate the ice retreat in late summer (February–March) when the modelled ice coverage shrinks to only about 30% of what is seen in the observations. In contrast, ACCESS1.3 produces more extensive ice coverage than the observations the year round. This deviation in ice extent between ACCESS-CM2 and ACCESS1.3 is inconsistent with the different SST biases near Antarctica shown in Fig. 4.

Fig. 7 shows the PI spin-up climatology of ACCESS1.3 and ACCESS-CM2 sea ice thickness in the summer season, i.e. July-September for NH and January–March for SH. For the NH summer, ACCESS-CM2 yields more extensive, though relatively thin (~0.25 cm), ice cover outside the observed 15% ice concentration boundary, particularly in the Barents Sea,

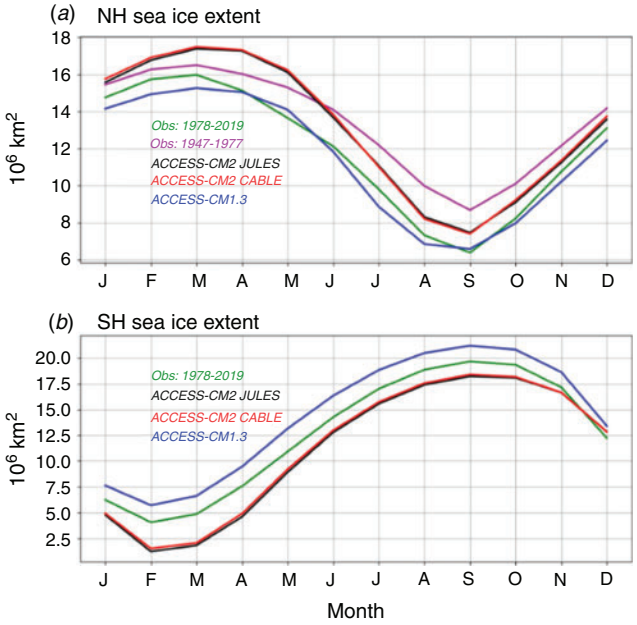

Fig. 6. Annual cycle climatology of sea ice extent (10^6 km^2) for: (*a*) NH, and (*b*) SH. Observations are from the HadISST (Rayner *et al.* 2003) sea ice concentration data for periods 1947–1977 and 1978–2019. Ice extent is defined as the total ocean area of grids that have ice concentration ≥15%.

Greenland Sea and Hudson Bay, as shown Fig. 7*b*. Also evident is that ACCESS-CM2 simulates slightly thicker sea ice than ACCESS1.3, although it is not unreasonable for ice to be 2.5–3 m thick across the central Arctic in summer, based on historical estimates of thickness of ice from submarine expeditions in the 1970s and 1980s (Yu *et al.* 2004; Kwok 2018), prior to the ice decline observed over the recent decades when much of the multi-year ice has disappeared (Comiso 2012; Kwok 2018).

For the SH summer, the ice extent off Antarctica in the ACCESS-CM2 PI spin-up is not extensive enough (as shown in Fig. 6*b*). Despite the improvements introduced to the Southern Ocean by the iceberg scheme (Section 3.2), the SSTs still exceed levels required for the realistic retention of sea ice in summer. The ice thickness in ACCESS-CM2 (Fig. 7*d*) no longer has a coastal band of (too) thick ice as seen in ACCESS1.3 (Fig. 7*c*), and the ice thickness pattern in the Weddell Sea is not realistic. Too little ice remains around the East Antarctic coast where the surface ocean is 2–3°C too warm in the January–March season. In contrast, ACCESS1.3 showed only small SST biases off Antarctica as seen in Fig. 4*b*, which resulted in the more extensive and unrealistically thick ice coverage.

4.5 Ocean interior

4.5.1 Global ocean temperature, salinity, and sea level

During the course of the spin-up, all three models undergo continuous thermal adjustment within the ocean interior. Fig. 8*a* shows the model drifts of annual mean global ocean volume-weighted temperature relative to the start of the selected 500-year period. For the two ACCESS-CM2 models, consistent with the larger positive TOA radiation budgets (Fig. 2*a*), the simulated

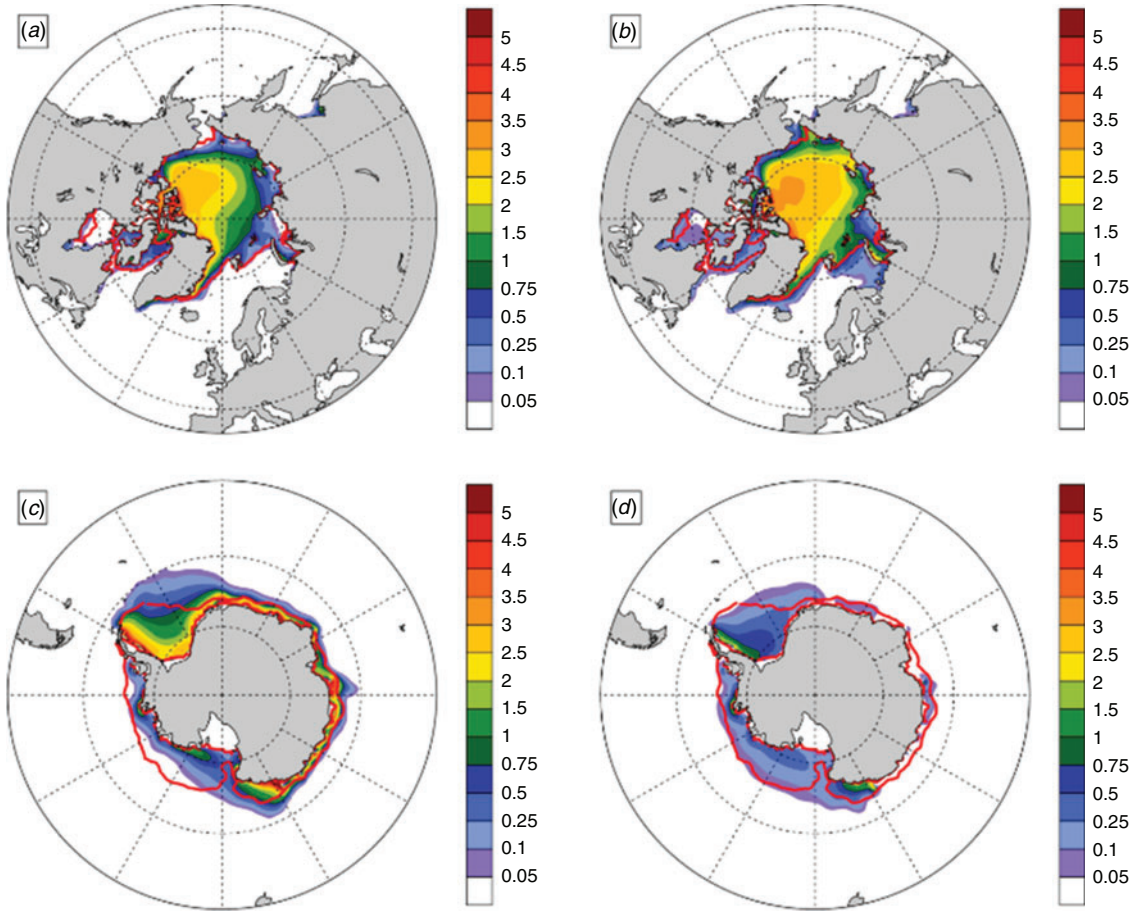

Fig. 7. Summer (July–September for NH and January–March for SH) sea ice thickness climatology (units: m) of PI spin-up simulations: (*a*) ACCESS1.3 NH, (*b*) ACCESS-CM2 NH, (*c*) ACCESS1.3 SH, and (*d*) ACCESS-CM2 SH. The thick red contour defines the 15% ice concentration boundary from the NSIDC observations (1978–2013 average) (Cavalieri *et al.* 1999; Fetterer *et al.* 2017).

earth system takes up the extra heat and stores it in the ocean. This heat uptake causes a considerable linear increase of the ocean temperature, with a total warming of ~0.41°C after 500 years. However, for ACCESS1.3, the ocean temperature drifts in the opposite direction and is ~0.16°C lower by the end of the 500-year period, despite a small positive radiation imbalance at the TOA during the whole integration period.

Examination of heat fluxes at the ocean surface shows a negative energy imbalance of about 0.1 W m^{-2} (i.e. ocean losing heat) in ACCESS1.3, which drives the cooling of the ocean interior but raises the question as to where the missing sink is in the energy budget to explain the heat loss. A similar concern is also found in the ACCESS-CM2 model, namely, the ocean uptakes less than 87% of the TOA radiation budget: the 0.4121°C global ocean warming shown in Fig. 8*a* for ACCESS-CM2 indicates an ocean heat uptake of about 2.265×10^{24} Joules. This amount of heat is only 86.7% of the system's net gain of energy which is approximately 2.613×10^{24} Joules, as implied by the (500-year mean) TOA net radiation imbalance of 0.4586 W m^{-2} (as shown in Fig. 2*a*). The remaining 13.3% of the heat gained would be too much to be stored anywhere in the system other than the ocean component. This indicates that there is an issue with energy conservation in the model which requires further investigation.

Fig. 8*b* shows the drift in annual mean volume-weighted global ocean salinity of the three models. ACCESS1.3 undergoes nearly linear salinity increase, indicating continuous loss of water mass from the ocean and thus the dropping of sea level height, as shown in Fig. 8*c*. In fact, the eventual increase of 0.00677 psu in global ocean salinity is equivalent to a sea level drop of about 70.2 cm, which is quite close to the 75 cm indicated by Fig. 8*c*. The ACCESS-CM2 models have a much better water mass balance, which is evidenced by very little change in the global ocean salinity and barystatic sea level height over the 500-year simulation. Particularly, ACCESS-CM2 maintains a very stable barystatic sea level height, which is noticeably better than the ACCESS-CM2j case. We note that, when the implied steric effect (expansion or contraction associated with change in the thermohaline state of the ocean) is considered, the (combined) sea level would see a rise of over 10 cm by the end of the 500-year ACCESS-CM2 simulations due to the 0.4°C warming in the ocean interior shown in Fig. 8*a*.

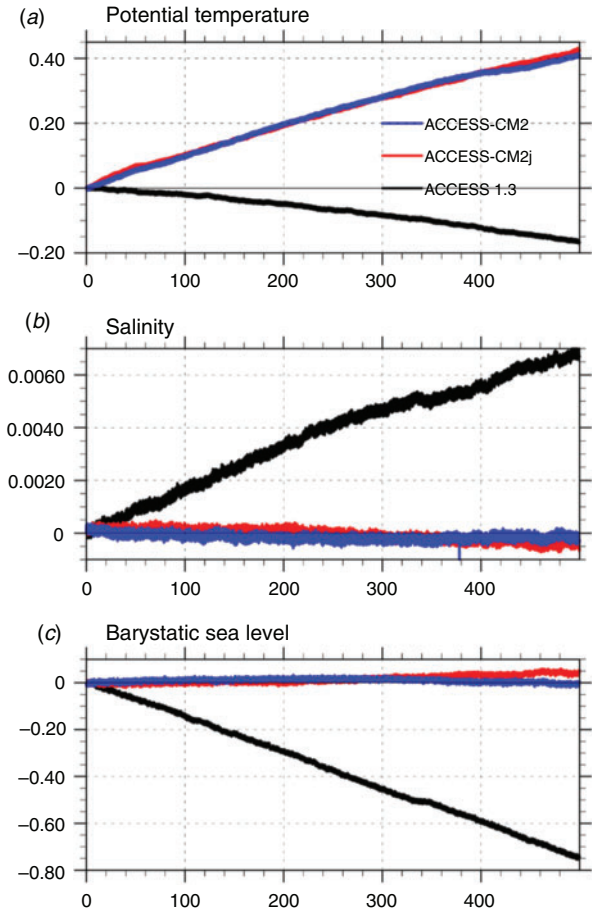

Fig. 8. Drift of annual mean global ocean: (*a*) temperature (°C), (*b*) salinity (psu), and (*c*) barystatic (mass induced) sea level height (m).

During the simulation, thermal changes in the ocean interior are not uniform through the depth, and salinity also undergoes continuous adjustment, although the ocean water mass and total salt are well conserved (see Fig. 10 and below). Changes in temperature and salinity are both strongly basin dependent and vary considerably with depth, as seen in Fig. 9, which shows the observations (Locarnini *et al.* 2010; Antonov *et al.* 2010) and model biases of the zonally averaged annual mean temperature and salinity (last 100-year mean) for ACCESS1.3 and ACCESS-CM2. ACCESS-CM2j is omitted here because of its strong similarity to ACCESS-CM2. Clearly ACCESS1.3 is somewhat too warm and saline in the subsurface north of 40–50°S, with the most evident errors located in the 0–40°N, 100–1200 m zone. ACCESS-CM2 shows significant thermal biases in a more extensive region (60°S–70°N, 200–3000 m) and generally negative salinity error in the upper ocean (above 600 m) except the narrow band just south of 40°N where a large positive saline error is generated due to the model's poor representation of the outflow from the Mediterranean Sea into the Atlantic Ocean through the Strait of Gibraltar.

It is worth noting that the large positive salinity bias of ACCESS1.3, centred at around 400 m depth, 10–20°N, extends too far south (Fig. 9*d*) and degrades the model's representation of the northward penetration of the Antarctic Immediate Water (AAIW) fresh tongue. The AAIW, formed at the ocean surface in the Antarctic convergence zone located 50–60°S, is a cold, relatively low salinity water mass found mostly at immediate depths in the Southern Ocean. The observed AAIW fresh tongue penetrates northward across the equator (Fig. 9*b*), which is simulated quite realistically in ACCESS-CM2 but not as well in ACCESS1.3 (data not shown).

Another notable difference between the ACCESS1.3 and ACCESS-CM2 simulations is found near Antarctica and in the abyssal ocean where ACCESS1.3 shows significant cooling biases, while ACCESS-CM2 has only minor cooling close to Antarctica with slight warming in the abyssal ocean. Along with the progress of the models' spin-up towards their individual equilibria (which may take thousands of years in the deep ocean), this contrast between the two models becomes larger over time. Fig. 10 shows the drifts (relative to the beginning of the periods considered) of horizontally averaged global ocean temperature and salinity of ACCESS1.3 and ACCESS-CM2. In ACCESS1.3 the ocean becomes warmer and saltier above 2000 m while below this there is cooling and freshening. In contrast, as shown in Fig. 10*c*, the ACCESS-CM2 model undergoes continuous warming at all depths except the top 400-m layer where a thermal (quasi-)equilibrium has been reached in the last 200 years. The strongest drift occurs at around 2000 m depth, with the largest warming being over 0.6°C within 500 years. Fig. 10*d* shows that salinity adjustment in ACCESS-CM2 is more complicated: both the upper (above 1000 m) and bottom (below 3000 m) oceans see freshening developing while the layer in between becomes saltier, with no sign of stabilisation yet. The ACCESS-CM2 abyssal ocean undergoes slow change (warming and freshening) as a result of the ocean circulations presented in Section 4.5.3.

4.5.2 Mixed layer depth

Mixed layer depth (MLD) is jointly determined by many atmospheric and oceanic processes such as wind-driven mixing, subduction, heat and water exchange between the atmosphere and ocean, and density-induced convective overturning. Here, the MLD is diagnosed from the simulated temperature and salinity using a criterion based on increase in density from the surface of 0.125 kg m^{-3} for the NH following Danabasoglu *et al.* (2014), and of 0.03 kg m^{-3} for the SH following Downes *et al.* (2015).

Fig. 11 presents the last 100-year average annual maximum MLD climatology of the ACCESS1.3 and ACCESS-CM2 PI spin-ups, along with the present-day observed estimate (Griffies *et al.* 2009). The annual maximum MLD in reality is attained in late winter and represents the deep mixing of surface waters that is associated with ocean water mass formation. Fig. 11*b, c* show that the two models simulate generally very similar geographical patterns in the global ocean except the Southern Ocean off Antarctica (Ross Sea and Weddell Sea) where ACCESS1.3 has very deep and extensive winter mixed layers (down to the ocean bottom) but ACCESS-CM2 does not. Compared with the observed estimate shown in Fig. 11*a*, the ACCESS-CM2 result is more realistic than that of ACCESS1.3 in the Southern Ocean, although it has a somewhat too extensive and deep maximum MLD along the Antarctic coast and overestimates the Ross sea convection.

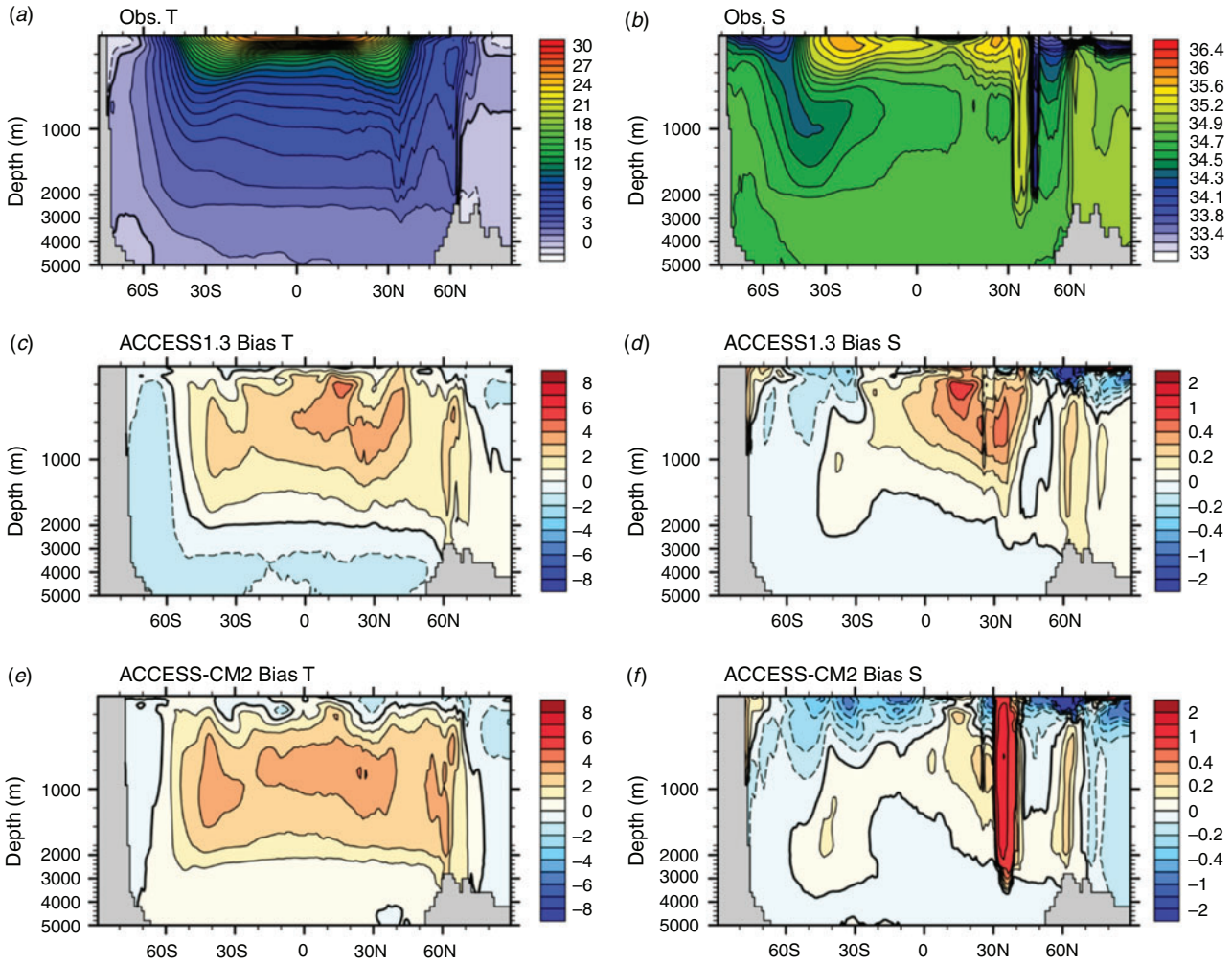

Fig. 9. Zonal average annual mean: (*a*) observed temperature, (*b*) observed salinity (contour interval is 0.2 for range ~33–34, 0.1 for range ~34–35, and 0.2 for the band beyond 35), (*c*) ACCESS1.3 temperature biases, (*d*) ACCESS1.3 salinity biases (contour interval is 0.1 for range –0.5 ~ 0.5, and 0.5 for bands beyond this range), (*e*) ACCESS-CM2 temperature biases, and (*f*) ACCESS-CM2 salinity biases (intervals are the same as in (*d*)). Units: temperature = °C, salinity = psu. Note the vertical coordinate (ocean depth) is stretched.

Along the northern flank of the Antarctic Circumpolar Current (ACC) in the Indian and Pacific oceans, observations show a long, narrow band of deep mixed layers which is associated with the Sub-Antarctic Mode Water formation and generally penetrates down to the depth of 300–700 m. The two models represent this band quite well but slightly overestimate the extent (and intensity) and produce a noticeable extension in the South Atlantic Ocean that does not exist in the observations. In the subpolar North Atlantic Ocean where the North Atlantic Deep Water (NADW) formation occurs, the observations show the winter deep mixing down to the depth of about 800 m. Both models misrepresent the location of the deepest mixing and spuriously exaggerate the intensity and extent of this deep mixing zone. In particular, ACCESS1.3 simulates the deepest mixing (over 4000 m) south of Greenland, associated with the large cold biases found there (Fig. 4*b*). In the northern part of the NH subtropical gyres, both models produce significantly deeper and more extensive maximum MLD than that seen in the observations. These regions are adjacent to the major frontal zones and prone to mis-presentation of the winds and surface buoyancy conditions.

4.5.3 Meridional overturning circulations

The ocean's meridional overturning circulation (MOC) connects the surface ocean and atmosphere with the huge reservoir of the deep ocean and is extremely important to the global climate system because of its critical role in transporting large amounts of water, heat, salt, carbon, nutrients and other substances around the globe. It is essential that a climate model be able to simulate realistic MOC patterns and strengths in the global ocean and individual ocean basins, particularly the Atlantic Ocean where the MOC is the central part of the global ocean conveyor belt. Fig. 12 presents the modelled global ocean and Atlantic Ocean MOC (AMOC) climatology of ACCESS1.3 and ACCESS-CM2, along with the temporal evolution of three important indices (representing water mass transports) over the 500-year period.

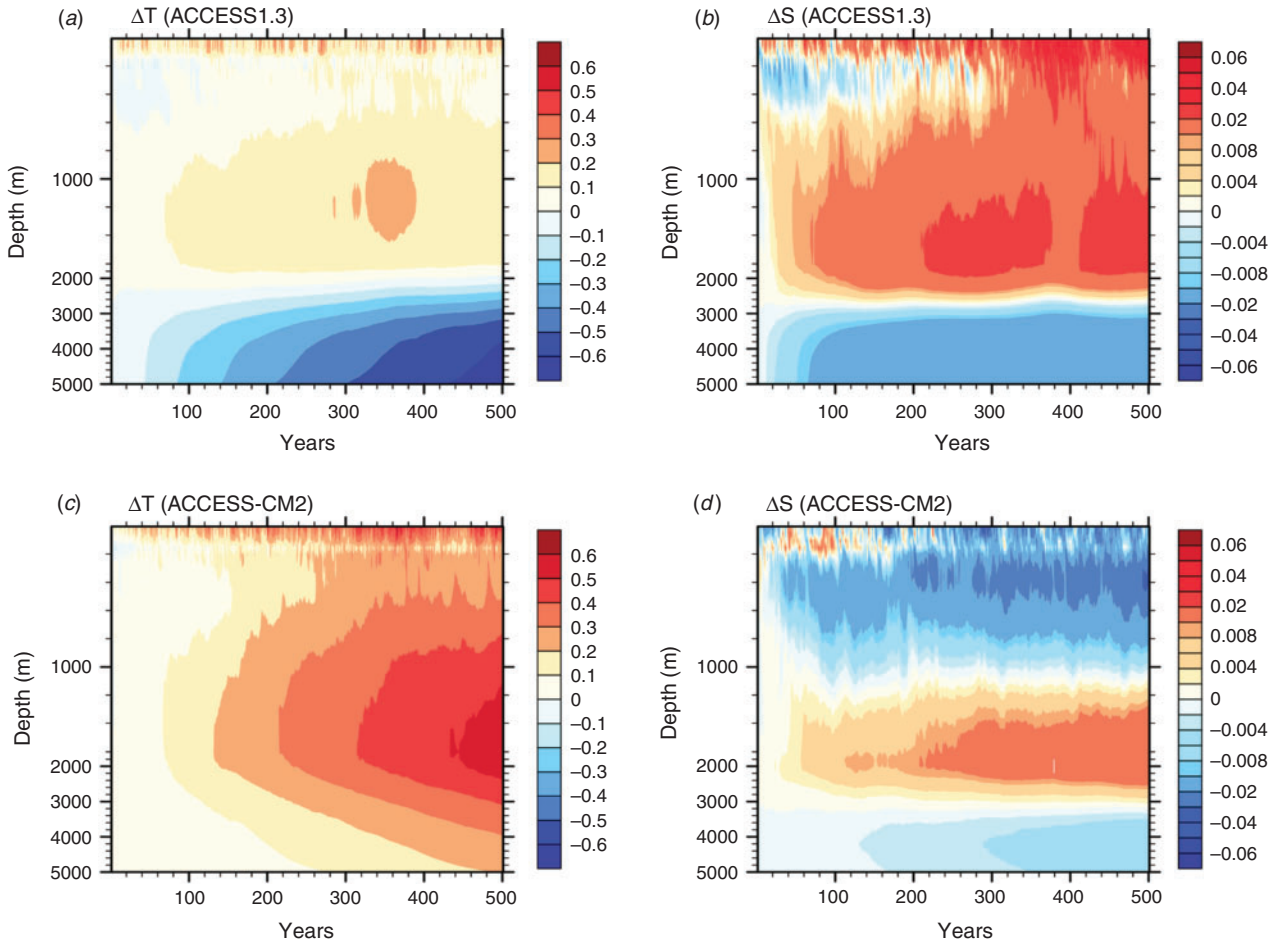

Fig. 10. Drifts of horizonal average annual mean: (*a*) ACCESS1.3 temperature, (*b*) ACCESS1.3 salinity, (*c*) ACCESS-CM2 temperature, and (*d*) ACCESS-CM2 salinity. Units: temperature = °C, salinity = psu. The vertical coordinate is stretched, and the contour interval is 0.002 for range –0.01 ~ 0.01, and 0.01 for bands beyond this range in (*b*) and (*d*).

Note the ACCESS-CM2j result was omitted because it has MOC patterns that are very similar to ACCESS-CM2.

The main features of the global ocean MOC (Fig. 12*b, d*) include the Antarctic Bottom Water (AABW) formation cell adjacent to Antarctica (centred around 68°S, 1000 m depth), an abyssal cell (centred around 3500 m depth, extending from Antarctica to the mid-latitudes of the NH), the tropical wind-driven cells (strong and shallow, beside the equator), the Deacon Cell driven by the SH sub-polar westerlies (centred around 60°S, penetrating to the depth of 2500 m in ACCESS-CM2 but to the bottom of the ocean in ACCESS1.3), and the NADW formation cell (centred around 45°N and 1000 m, penetrating to the depth of around 3000 m). We note that the Deacon cell in the Southern Ocean is an indirect cell that is apparent when the zonal mean MOC is calculated in height coordinates, but does not appear (or is substantially reduced) if the MOC is calculated in density coordinates (e.g. Doos and Webb 1994; Hirst *et al.* 1996). While producing generally similar patterns of MOC in both the global ocean and Atlantic Ocean, the two models evidently differ from each other in representing the Deacon cell and the Southern Ocean abyssal cell.

Fig. 12*b* shows a very strong abyssal circulation in ACCESS1.3 which, together with the spuriously deep and extensive convection off Antarctica (Ross Sea and Weddell Sea, see Fig. 11*b*), is responsible for ventilating the abyssal ocean with the cold and fresh AABW, explaining the large cooling and freshening in the abyssal ocean of ACCESS1.3 (e.g. Figs. 10*a, b*). In the ACCESS-CM2 case, the AABW is transported northwards by a milder abyssal circulation which ventilates the bottom ocean, and the abyssal ocean shows much more moderate drift in both salinity and temperature (Fig. 10*c, d*).

Fig. 12*e* shows that, with evident decadal variability, the NADW intensity and the maximum AMOC transport at 26°N are stabilised at around 22 Sv and 18 Sv, respectively, for both models. This modelled NADW intensity is considerably stronger than the estimated value of ~15 Sv from observations (e.g. Ganachaud and Wunsch 2000; Ganachaud 2003; Lumpkin *et al.* 2008). The modelled AMOC at 26°N is well within the range of RAPID array at 26°N observation (McCarthy *et al.* 2015; Smeed *et al.* 2018) although the observations show significant interannual variability and a sudden drop of the transport around 2008. For example, Smeed *et al.* (2018) showed that the AMOC

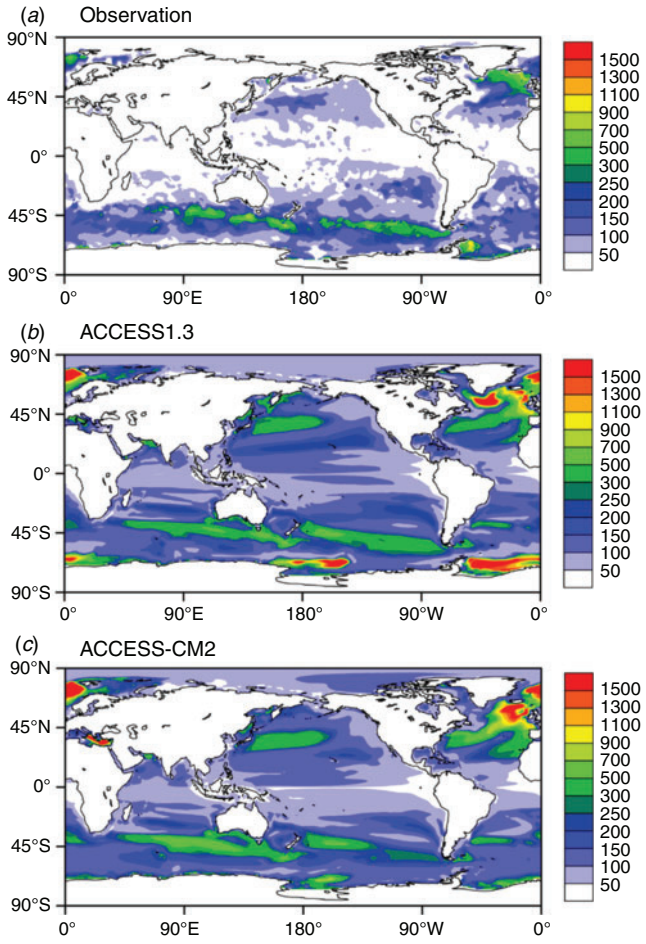

Fig. 11. Annual maximum mixed layer depth (m): (*a*) observation (Griffies *et al.* 2009), (*b*) ACCESS1.3, and (*c*) ACCES-CM2. Model results are from the last 100-year average.

transport at 26°N was ~17–20.5 Sv before 2008, dipped to a minimum of 12 Sv at around 2010 and then generally fluctuated between 15 and 17 Sv thereafter.

Similarly, as shown in Fig. 12*f*, the AABW formation cell in both models evolves with decadal variability, with a mean of ~11 Sv in ACCESS1.3 and ~12 Sv in ACCESS-CM2 which may be significantly lower than the present-day observations. For example, Naveira Garabato *et al.* (2002) reported a diagnosed AABW formation of 9.7 ± 3.9 Sv in the Weddell Sea alone, and Talley (2013) gave an estimate of 29 Sv of the total AABW formation.

4.5.4 Barotropic flows

Fig. 13*a, b* show the barotropic streamfunction climatology maps of the ACCESS1.3 and ACCESS-CM2 spin-ups, respectively. The barotropic streamfunction depicts the vertically integrated horizontal water mass transport by the major currents and gyres, which are all primarily wind-driven, of the global ocean. Both models produce reasonable patterns of the global ocean barotropic flows and represent quite well the major currents and gyres, such as the very strong ACC which is the only flow connecting the Indian, Pacific and Atlantic oceans, as well as strong anti-cyclonic subtropical gyres in the three major oceans that depict the western boundary currents and cyclonic subpolar and tropical gyres.

Despite the general similarity of the distributional patterns in the two maps, there are some noticeable differences between them. For example, the Gulf Stream (western boundary currents) in the North Atlantic is slightly weaker in ACCESS-CM2 than in ACCESS1.3. However, the maximum transport rate of about 30 Sv in both models is in good accordance with the observed estimate, which was ~32–35 Sv before 2008 and fluctuated around 32.5 Sv thereafter at 26°N, from the RAPID-WATCH project (Smeed *et al.* 2018). We note that although the models produce realistic transport of the Gulf Stream inflow, the simulated western boundary currents are too wide and slow to exhibit realistic inertial behaviour in their outflows because of the low resolution (Kiss *et al.* 2020, and reference therein).

Further north, the simulated subpolar gyres in ACCESS1.3 (ACCESS-CM2) give a maximum transport of 17 (26) Sv in the North Pacific Ocean and 45 (29) Sv in the North Atlantic Ocean, respectively, and their counterparts from observational estimates are 32 Sv (Colin de Verdière and Ollitrault 2016) and ~25–40 Sv (Clarke 1984; Bacon 1997). We see that ACCESS-CM2 matches the observations better than ACCESS1.3, and this difference is of climatic significance. A stronger subpolar cyclonic gyre transports more cold water from north to south and pushes back the poleward intrusion of warm water brought from the south by the subtropical gyre and vice versa. For ACCESS1.3, the subpolar cyclonic gyre is too strong in the North Atlantic but too weak in the North Pacific, and consequently the model sees large cold biases and spuriously deep mixing south of Greenland (Figs. 4*b*, 11*b*) but strong warm biases northeast of Japan (Fig. 4*b*). These thermal biases are largely reduced in ACCESS-CM2 (Fig. 4*c*), associated with a more reasonable representation of the subpolar cyclonic gyre than in ACCESS1.3. In the North Pacific Ocean ACCESS-CM2 sees the poleward Kuroshio Current turn east earlier than that in ACCESS1.3, which results in significant improvement of the SST simulation in that region (see Fig. 4*b, c*).

The ACC is the most important current in the Southern Ocean and the strongest in the world oceans. It is the only current that flows completely around the globe, encircling the Antarctic continent. The ACC is an eastward flow primarily driven by the strong westerly winds and is in approximately geostrophic balance with the meridional density gradient in the Southern Ocean (e.g. Bi *et al.* 2002). Fig. 13*c* shows the evolution of the ACC transport through Drake Passage simulated in the 3 models. While undergoing noticeable decadal oscillation, the ACC is stabilised in ACCESS-CM2 and ACCESS-CM2j at a level (~185–188 Sv) just above the observational range (173 ± 11 Sv; Donohue *et al.* 2016), but in ACCESS1.3 drifts to a considerably higher level, reaching 200 Sv by the end of the run. In fact, the ACC transport in ACCESS-CM2j increases from around 150 Sv to over 180 Sv within the first 200 years of the spin-up (not shown) and stabilises thereafter; ACCESS-CM2 starts from the end of year 200 of ACCESS-CM2j and only sees a short and small increase of ACC at the start and then stabilises; ACCESS1.3 has a continuous increase in the ACC transport through the whole 750-year integration. That ACCESS1.3 produces higher ACC transport than ACCESS-CM2 likely

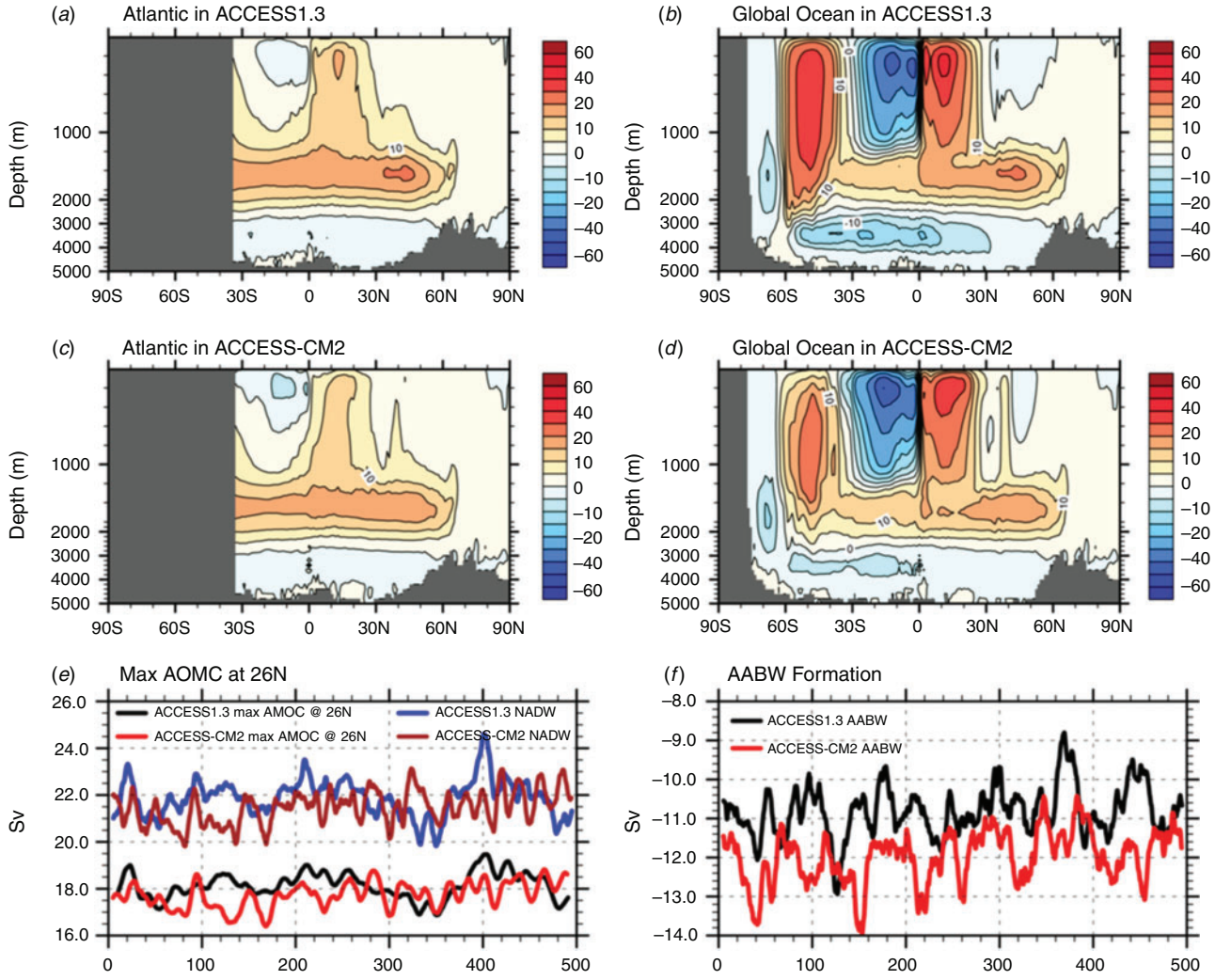

Fig. 12. Climatology of meridional overturning circulations of: (*a*) Atlantic in ACCESS1.3, (*b*) Global ocean in ACCESS1.3, (*c*) Atlantic in ACCESS-CM2, (*d*) Global ocean in ACCESS-CM2, and evolution of: (*e*) max AMOC at 26°N and the NADW formation, (*f*) Antarctic Bottom Water (AABW) formation. Units: $Sv = 10^6\ m^3\ s^{-1}$. In (*a–d*), the vertical coordinate is stretched, and the contour interval is 5 for range –20 ~ 20 and 10 for other bands.

results from the difference in buoyancy biases between the two models in the Southern Ocean. As shown in Fig. 9*b–f*, although the two models show generally similar salinity biases in the high latitudes water column in the Southern Ocean, ACCESS1.3 has noticeably stronger temperature contrast cross 60°S than ACCESS-CM2, allowing for a stronger meridional density gradient in the water column cross ACC for ACCESS1.3, which requires stronger ACC flow to maintain the geostrophic balance (Bi *et al.* 2002).

4.6 El Nino Southern Oscillation

El Nino Southern Oscillation (ENSO) is a coupled ocean-atmosphere phenomenon, a dominant mode of interannual variability found in the Pacific Ocean that exerts great impacts on weather, climate and ecological system worldwide. As one of the most influential natural phenomena, ENSO has been an important indicator for evaluating coupled models' performance in climate simulation (e.g. Leloup *et al.* 2008; Bellenger *et al.* 2014). Here we provide a basic evaluation of the modelled ENSO in ACCESS-CM2 and ACCESS1.3 by comparing the ENSO variability (tropical Pacific SST standard deviation), variance and frequency (power spectra) against that from the 1990–2014 HadISST observations (Rayner *et al.* 2003). Detailed analysis and evaluation of the ACCESS-CM2 ENSO simulation with more complicated metrics will be presented in future papers.

As shown in Fig. 14*a*, ENSO is characterised by large-scale anomalous SST warming (El Nino)/cooling (La Nina) in the tropical central eastern Pacific, with the largest variability (RMSE > 1°C) located at around 105°W on the equator. The ACCESS models generally depict such a feature but show noticeable differences. ACCESS1.3 simulates the large variability centre (with maximum RMSE of about 1.3°) at around 0°N, 110°W, and the westward extension of this centre is too far west, reaching the maritime continent and forms another high variability centre in

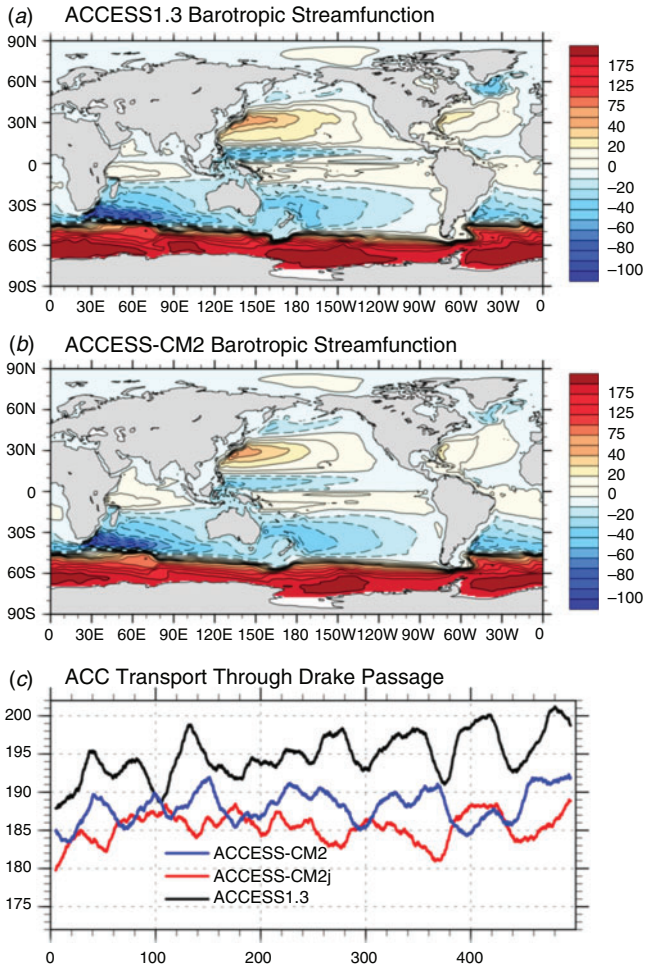

Fig. 13. Barotropic Streamfunction (last 50-year mean) of: (*a*) ACCESS1.3; (*b*) ACCESS-CM2, and (*c*) evolution of models' ACC transport through Drake Passage. Units: Sv = 10^6 m^3 s^{-1}. Note the uneven contour intervals in (*a*) and (*b*): 10 and 25 for bands –100 ~ 50 and 75 ~ 200, respectively.

the tropical western Pacific (Fig. 14*b*). Such unrealistic spatial pattern of ENSO variability is associated with the models' cold biases in the tropical Pacific Ocean (e.g. Samanta *et al.* 2018) as shown in Fig. 4*b*. For ACCESS-CM2 (Fig. 14*c*), the ENSO variability is even higher (maximum RMSE > 2°C) and centred further west on the equator (at 115°W). However, the westward extension of this variability is more like the observations than ACCESS1.3 and there is no second variability peak in the west, which is a notable improvement of ACCCESS-CM2 in simulating the ENSO variability pattern.

Fig. 14*d* shows the observed Nino 3 SST anomaly power spectra for the period of 1900–2014, which indicates the SST oscillations between warming and cooling on a time scale of 3–7 years. ACCESS-CM2 fails to produce strong enough variance (power) over the dominant frequency range (i.e. >3 years, as shown by the observation) in all the three 100-year time slices (Fig. 14*f*), and generally presents regular quasi-biennial oscillations of the Nino 3 SST. ACCESS1.3 (Fig. 14*e*) on the other hand simulates somewhat too strong variance in the 3–4 year time scale for one of the 3 time slices but shows quite realistic power spectrum for another time slice (red curve) which presents two variance peaks at 3-year and >4-year time scales, respectively, and overall has a much better power spectrum than the ACCESS-CM2 simulation.

5 Concluding summary

Two versions of the new generation ACCESS coupled model, ACCESS-CM2 which uses CABLE2.5 as the land surface model and ACCESS-CM2j, which is configured with the JULES land surface scheme, have been used in parallel to conduct long spin-up simulations under preindustrial atmospheric conditions as part of preparations for the ACCESS-CM2 submission to CMIP6. This study describes the model configuration and provides a basic assessment of the model's PI spin-up climate, with a focus on the results for the official version ACCESS-CM2.

By comparing the ACCESS-CM2 and ACCESS1.3 PI spin-up results against the present-day observations where applicable, we see some significant improvements in ACCESS-CM2 over the CMIP5 model ACCESS1.3, including the following.

- Good closure of water mass conservation – contrasting to a faulty, constant water loss from the world oceans in ACCESS1.3, ACCESS-CM2 has very good hydrological balance which leads to very stable global barystatic sea level height over the course of the spin-up simulation.
- Better simulation of precipitation over land – model error of ACCESS-CM2 is only 1/3 of that seen in ACCESS1.3.
- Better representation of the Antarctic Intermediate Water (AAIW) – the characteristic northward extension of the AAIW subsurface fresh tongue is in much closer agreement with the observations.
- More realistic meridional overturning circulations in deep ocean – ACCESS-CM2 simulates an abyssal circulation with milder strength, resulting in reasonable ventilation. Thus ACCESS-CM2 does not show the cooling and freshening drift in the bottom ocean seen in ACCESS1.3.
- Better barotropic flows – ACCESS-CM2 simulates more realistic strength and position of the subpolar cyclonic gyres in both the North Atlantic and North Pacific. This improvement results in smaller SST biases in the subpolar frontal zones, which is very likely the reason for the model avoiding the spuriously deep mixing south of Greenland seen in ACCESS1.3. Also notable is that the Antarctic Circumpolar Current transport in ACCESS-CM2 is more stable and closer to observations.

Meanwhile, we see noticeable worsening in some aspects of the ACCESS-CM2 simulation relative to ACCESS1.3, such as the following.

- Larger imbalance of radiation budget at the top of atmosphere – this is partly reflected in the linear increase of the global ocean average temperature; however, it significantly exceeds the continuous heat uptake in the ocean due to an energy conservation issue.
- Larger sea surface warm biases in the Southern Ocean, particularly the Antarctic coastal regions – in association with this, ACCESS-CM2 simulates somewhat smaller extent and too thin Antarctic sea ice, especially in the summer season.

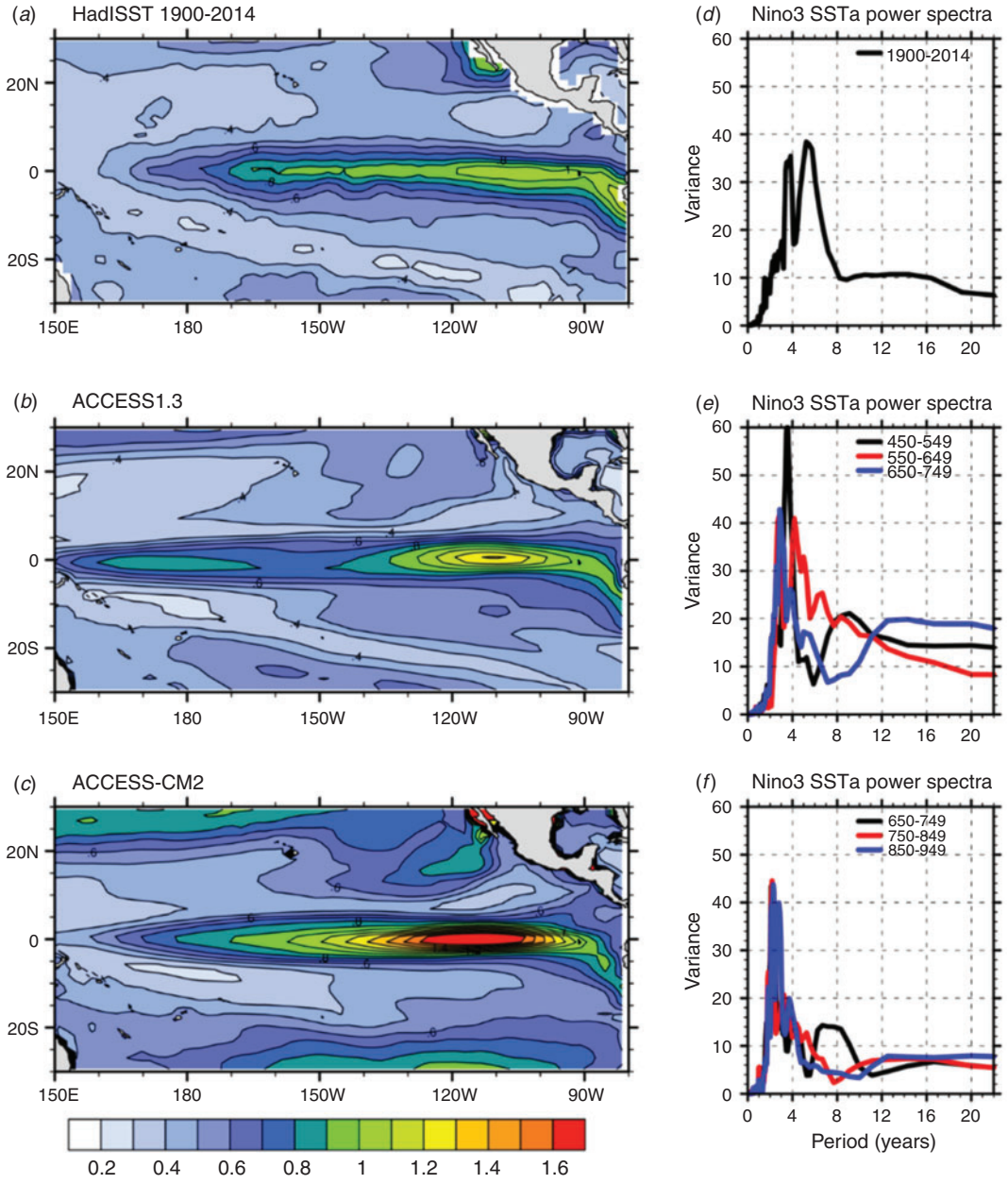

Fig. 14. Left panels – Tropical Pacific SST standard deviation (°C) of: (*a*) the 1900–2014 HadISST data, (*b*) the last 300-year model result for ACCESS1.3, (*c*) same as (*b*) but for ACCESS-CM2. Right panels – Nino 3 (90–150°W, 5°S–5°N) SST anomaly power spectra of: (*d*) the 1900–2014 HadISST data, (*e*) three consecutive 100-year time slices of the last 300-year simulation of ACCESS1.3, (*f*) same as (*e*) but for ACCESS-CM2.

- Large fresh biases at the sea surface – despite very good hydrological balance and thus stable global ocean average salinity, the surface ocean overall sees a significant drop in salinity.
- ENSO is a too regular quasi-biennial event.

We note that this assessment of the ACCESS-CM2 PI spin-up simulations in this study is predominantly focussed on the ocean climate. This is because the ocean is the slowest component to equilibrate across the spin-up run and hence sets the basis for a stable control simulation. More comprehensive assessments of the model performance in climate simulations covering all model components will be done based on the CMIP6 *historical* and *piControl* simulations and will be presented in future papers.

Conflicts of interest

The authors declare that they have no conflicts of interest.

Acknowledgements

This project is jointly funded through CSIRO and the Earth Systems and Climate Change Hub of the Australian Government's National Environmental Science Program. The computation for this work was performed using the NCI National Facility at the Australian National University, and we particularly thank Dr Ben Evans and the associated NCI staff members for their support. We further thank Cath Senior, David Storkey, Richard Hill and other colleagues at the Met Office for helpful discussions during the course of this work, and João Teixeira and Charline Marzin for model forcing data and HadGEM-GC3.1 model output fields useful for comparison and benchmarking. We thank Marcus Thatcher for his comments on a pre-submission draft. Particularly, we thank Australian Research Council Centre of Excellence for Climate Extremes for providing the "harmonised" code of MOM5 for ACCESS-CM2 implementation. We acknowledge the World Climate Research Programme, which, through its Working Group on Coupled Modelling, coordinated and promoted CMIP6. We thank the Earth System Grid Federation (ESGF) for archiving the data and providing access, and the multiple funding agencies who support CMIP6 and ESGF.

References

Adcroft, A., and Campin, J.-M. (2004). Rescaled height coordinates for accurate representation of free-surface flows in ocean circulation models. *Ocean Modell* **7**, 269–284. doi:10.1016/J.OCEMOD.2003.09.003

Adler, R. F., Sapiano, M. R. P., Huffman, G. J., Wang, J.-J., Gu, G., Bolvin, D., Chiu, L., Schneider, U., Becker, A., Nelkin, E., Xie, P., Ferraro, R., and Shin, D.-B. (2018). The Global Precipitation Climatology Project (GPCP) Monthly Analysis (New Version 2.3) and a Review of 2017 Global Precipitation. *Atmosphere* (2018). **9**(4), 138. doi:10.3390/ATMOS9040138

Allan, R. P., Liu, C., Loeb, N. G., Palmer, M. D., Roberts, M., Smith, D., and Vidale, P. L. (2014). Changes in global net radiative imbalance 1985–2012. *Geophys. Res. Lett.* **41**, 5588–5597. doi:10.1002/2014GL060962

Antonov, J. I., Locarnini, R. A., Boyer, T. P., Mishonov, A. V. and Garcia, H. E. (2006). 'World Ocean Atlas 2005, Vol. 2: Salinity. NOAA Atlas NESDIS 62.' (Ed. S. Levitus.) (U.S. Government Printing Office: Washington, D.C.)

Antonov, J. I., Seidov, D., Boyer, T. P., Locarnini, R. A., Mishonov, A. V., Garcia, H. E., Baranova, O. K., Zweng, M. M. and Johnson, D. R. (2010). 'World Ocean Atlas 2009, Vol. 2: Salinity. NOAA Atlas NESDIS 69.' (Ed. S. Levitus.), (U.S. Government Printing Office: Washington, D.C.)

Arakawa, A. and Lamb, V. R. (1977). Computational design and the basic dynamical processes of the UCLA general circulation Model. In 'Methods in Computational Physics: Advances in Research and Applications, Vol. 17'. (Ed. J. Chang.) pp. 173–265. (Elsevier.) doi:10.1016/B978-0-12-460817-7.50009-4

Arribas, A., Glover, M., Maidens, A., Peterson, K., Gordon, M., MacLachlan, C., Cusack, S., and Scaife, A. (2011). The GloSea4 ensemble prediction system for seasonal forecasting. *Mon. Wea. Rev.* **139**, 1891–1910. doi:10.1175/2010MWR3615.1

Bacon, S. (1997). Circulation and fluxes in the North Atlantic between Greenland and Ireland. *J. Phys. Oceanogr.* **27**, 1420–1435. doi:10.1175/1520-0485(1997)027<1420:CAFITN>2.0.CO;2

Bellouin, N., Rae, J., Jones, A., Johnson, C., Haywood, J., and Boucher, O. (2011). Aerosol forcing in the Climate Model Intercomparison Project (CMIP5) simulations by HadGEM2-ES and the role of ammonium nitrate. *J. Geophys. Res.* **116**, D20206. doi:10.1029/2011JD016074

Best, M. J., Pryor, M., Clark, D. B., Rooney, G. G., Essery, R. L. H., Ménard, C. B., Edwards, J. M., Hendry, M. A., Porson, A., Gedney, N., Mercado, L. M., Sitch, S., Blyth, E., Boucher, O., Cox, P. M., Grimmond, C. S. B., and Harding, R. J. (2011). The Joint UK Land Environment Simulator (JULES), model description – Part 1: Energy and water fluxes. *Geosci. Model Dev.* **4**, 677–699. doi:10.5194/GMD-4-677-2011

Bi, D. and Marsland, S. J. (2010). Australian Climate Ocean Model (AusCOM) Users Guide. CAWCR Technical Report No. 027. The Centre for Australian Weather and Climate Research, a partnership between CSIRO and the Bureau of Meteorology.

Bi, D., Budd, W. F., Hirst, A. C., and Wu, X. (2002). Response of the Antarctic Circumpolar Current to global warming forcing in the CSIRO coupled model. *Geophys. Res. Lett.* **29**(24), 2173. doi:10.1029/2002GL015919

Bi, D., Marsland, S. J., Uotila, P., O'Farrell, S., Fiedler, R., Sullivan, A., Griffies, S. M., Zhou, X., and Hirst, A. C. (2013*a*). ACCESSOM: the ocean and sea-ice core of the ACCESS coupled model. *Aust. Meteor. Oceanogr. J.* **63**, 213–232. doi:10.22499/2.6301.014

Bi, D., Dix, M., Marsland, S. J., O'Farrell, S., Rashid, H. A., Uotila, P., Hirst, A. C., Kowalczyk, E., Golebiewski, M., Sullivan, A., Yan, H., Hannah, N., Franklin, C., Sun, Z., Vohralik, P., Watterson, I., Zhou, X., Fiedler, R., Collier, M., Ma, Y., Noonan, J., Stevens, L., Uhe, P., Zhu, H., Griffies, S. M., Hill, R., Harris, C., and Puri, K. (2013*b*). The ACCESS coupled model: description, control climate and evaluation. *Aust. Meteor. Oceanogr. J.* **63**, 41–64. doi:10.22499/2.6301.004

Bellenger, H., Guilyardi, E., Leloup, J., Lengaigne, J., and Vialard, J. (2014). ENSO representation in climate models: from CMIP3 to CMIP5. *Climate Dyn.* **42**, 1999–2018. doi:10.1007/S00382-013-1783-Z

Bitz, C. M., and Lipscomb, W. H. (1999). An energy-conserving thermodynamic model of sea ice. *J. Geophys. Res.-Oceans* **104**, 15669–15677. doi:10.1029/1999JC900100

Brown, A. R., Beare, R. J., Edwards, J. M., Lock, A. P., Keogh, S. J., Milton, S. F., and Walters, D. N. (2008). Upgrades to the boundary-layer scheme in the Met Office numerical weather prediction model. *Bound.-Lay. Meteorol.* **128**, 117–132. doi:10.1007/S10546-008-9275-0

Boutle, I. A., and Morcrette, C. J. (2010). Parametrization of area cloud fraction. *Atmos. Sci. Lett.* **11**, 283–289. doi:10.1002/ASL.293

Boyer, T., Locarnini, R. A., Zweng, M. M.,. Mishonov, A. V. Reagan, J. R., Antonov, J. I. Garcia, H. E., Baranova, O. K., Johnson, D. R., Seidov, D., Biddle, M. M. and Hamilton, M. (2015). 'Changes to calculations of the World Ocean Atlas 2013 for version 2.' (National Oceanographic Data Center: Silver Spring.)

Cavalieri, D. J., Parkinson, C. L., Gloersen, P., Comiso, J. C., and Zwally, H. J. (1999). Deriving long-term time series of sea ice cover from satellite passive-microwave multisensor data sets. *J. Geophys. Res.* **104**, 15803–15814. doi:10.1029/1999JC900081

Charney, J. G., and Phillips, N. A. (1953). Numerical integration of the quasi-geostrophic equations for barotropic and simple baroclinic flows. *J. Meteor.* **10**, 71–99. doi:10.1175/1520-0469(1953)010<0071:NIOTQG>2.0.CO;2

Cinquini, L., Crichton, D., Mattmann, C., Harney, J., Shipman, G., Wang, F., Ananthakrishnan, R., Miller, N., Denvil, S., Morgan, M., Pobre, Z., Bell, G. M., Doutriaux, C., Drach, R., Williams, D., Kershaw, P., Pascoe, S., Gonzalez, E., Fiore, S., and Schweitzer, R. (2014). The Earth System Grid Federation: An open infrastructure for access to distributed geospatial data. *Future Gener. Comp. Syst.* **36**, 400–417. doi:10.1016/J.FUTURE.2013.07.002

Clark, D. B., Mercado, L. M., Sitch, S., Jones, C. D., Gedney, N., Best, M. J., Pryor, M., Rooney, G. G., Essery, R. L. H., Blyth, Boucher, O., Cox, P. M., and Harding, R. J. (2011). The Joint UK Land Environment Simulator (JULES), model description – Part 2: Carbon fluxes and vegetation. *Geosci. Model Dev.* **4**, 701–722. doi:10.5194/GMD-4-701-2011

Clarke, R. A. (1984). Transport through the Cape Farewell–Flemish Cap section. *Rapp. P.-V. Reun.- Cons. Int. Explor. Mer.* **185**, 120–130.

Colin de Verdière, A., and Ollitrault, M. (2016). A direct determination of the World Ocean barotropic circulation. *J. Phys. Oceanogr.* **46**(1), 255–273. doi:10.1175/JPO-D-15-0046.1

Collins, M., Booth, B. B. B., Bhaskaran, B., Harris, G. R., Murphy, J. M., Sexton, D. M. H., and Webb, M. J. (2010). Climate model errors, feedbacks and forcings: A comparison of perturbed physics and multi-model ensembles. *Climate Dyn.* **36**(9–10), 1737–1766. doi:10.1007/S00382-010-0808-0

Comiso, J. (2012). Large Decadal Decline of the Multi-year ice cover. *J. Climate* **25**, 1176–1193. doi:10.1175/JCLI-D-11-00113.1

Cracknell, A. P., Newcombe, S. K., Black, A. F., and Kirby, N. E. (2001). The ABDMAP (Algal Bloom Detection, Monitoring and Prediction) Concerted Action. *Int. J. Remote Sens.* **22**, 205–247. doi:10.1080/014311601449916

Craig, A., Valcke, S., and Coquart, L. (2017). Development and performance of a new version of the OASIS coupler, OASIS3-MCT_3.0. *Geosci. Model Dev.* **10**, 3297–3308. doi:10.5194/GMD-10-3297-2017

Danabasoglu, G., Yeager, S. G., Bailey, D., Behrens, E., Bentsen, M., Bi, D., Biastoch, A., Böning, C., Bozec, A., Canuto, V. M., Cassou, C., Chassignet, E., Coward, A. C., Danilov, S., Diansky, N., Drange, H., Farneti, R., Fernandez, E., Fogli, P. G., Forget, G., Fujii, Y., Griffies, S. M., Gusev, A., Heimbach, P., Howard, A., Jung, T., Kelley, M., Large, W. G., Leboissetier, A., Lu, J., Madec, G., Marsland, S. J., Masina, S., Navarra, A., Nurser, A. J. G., Pirani, A., Salas y Mélia, D., Samuels, B. L., Scheinert, M., Sidorenko, D., Treguier, A.-M., Tsujino, H., Uotila, P., Valcke, S., Voldoire, A., and Wang, Q. (2014). North Atlantic simulations in Coordinated Ocean-ice Reference Experiments phase II (CORE-II). Part I: Mean states. *Ocean Model* **73**, 76–107. doi:10.1016/J.OCEMOD.2013.10.005

Davies, T., Cullen, M. J. P., Malcolm, A. J., Mawson, M. H., Staniforth, A., White, A. A., and Wood, N. (2005). A new dynamical core for the Met Office's global and regional modelling of the atmosphere. *Quart. J. Roy. Meteor. Soc* **131**, 1759–1782. doi:10.1256/QJ.04.101

Dix, M., Vohralik, P., Bi, D., Rashid, H., Marsland, S., O'Farrell, S., Uotila, P., Hirst, T., Kowalczyk, E., Sullivan, A., Yan, H., Franklin, C., Sun, Z., Watterson, I., Collier, M., Noonan, J., Rotstayn, L., Stevens, L., Uhe, P., and Puri, K. (2013). The ACCESS coupled model: documentation of core CMIP5 simulations and initial results. *Aust. Meteor. Oceanogr. J.* **63**, 83–99. doi:10.22499/2.6301.006

Donohue, K. A., Tracey, K. L., Watts, D. R., Chidichimo, M. P., and Chereskin, T. K. (2016). Mean Antarctic circumpolar current transport measured in Drake passage. *Geophys. Res. Lett.* **43**, 11760–11767. doi:10.1002/2016GL070319

Doos, K., and Webb, D. J. (1994). The Deacon Cell and other meridional cells of the Southern Ocean. *J. Phys. Ocean* **24**, 429442.

Downes, S. M., Farneti, R., Uotila, P., Griffies, S. M., Marsland, S. J., Bailey, D., Behrens, E., Bentsen, M., Bi, D. H., Biastoch, A., Boning, C., Bozec, A., Canuto, V. M., Chassignet, E., Danabasoglu, G., Danilov, S., Diansky, N., Drange, H., Fogli, P. G., Gusev, A., Howard, A., Ilicak, M., Jung, T., Kelley, M., Large, W. G., Leboissetier, A., Long, M., Lu, J. H., Masina, S., Mishra, A., Navarra, A., Nurser, A. J. G., Patara, L., Samuels, B. L., Sidorenko, D., Spence, P., Tsujino, H., Wang, Q., and Yeager, S. G. (2015). An assessment of Southern Ocean water masses and sea ice during 1988–2007 in a suite of interannual CORE-II simulations. *Ocean Model* **94**, 67–94. doi:10.1016/J.OCEMOD.2015.07.022

Edwards, J. M., and Slingo, A. (1996). Studies with a flexible new radiation code. I: Choosing a configuration for a large-scale model. *Quart. J. Roy. Meteor. Soc.* **122**, 689–719. doi:10.1002/QJ.49712253107

Eyring, V., Bony, S., Meehl, G. A., Senior, C., Stevens, B., Stouffer, R. J., and Taylor, K. E. (2016). Overview of the Coupled Model Intercomparison Project Phase 6 (CMIP6) experimental design and organisation. *Geosci. Model Dev.* **9**, 1937–1958. doi:10.5194/GMD-9-1937-2016

Fairall, C. W., Bradley, E. F., Hare, J. E., Grachev, A. A., and Edson, J. B. (2003). Bulk parameterization of air-sea fluxes: updates and verification for the COARE algorithm. *J. Climate* **16**, 571–591. doi:10.1175/1520-0442(2003)016<0571:BPOASF>2.0.CO;2

Ferrari, R., Griffies, S. M., Nurser, A. J. G., and Vallis, G. K. (2010). A boundary-value problem for the parameterized mesoscale eddy transport. *Ocean Model* **32**, 143–156. doi:10.1016/J.OCEMOD.2010.01.004

Fetterer, F., Knowles, K., Meier, W., Savoie, M., and Windnagel, A. K. (2017). 'Sea Ice Index, Version 3, Tech. Rep.' (NSIDC, National Snow and Ice Data Center: Boulder, Colorado, USA.) Available at https://doi.org/10.7265/N5K072F8.

Flato, G., Marotzke, J., Abiodun, B., Braconnot, P., Chou, S. C., Collins, W., Cox, P., Driouech, F., Emori, S., Eyring, V., Forest, C., Gleckler, P., Guilyardi, E., Jakob, C., Kattsov, V., Reason C. and Rummukainen M. (2013). Evaluation of Climate Models. In: Climate Change 2013: The Physical Science Basis. Contribution of Working Group I to the Fifth Assessment Report of the Intergovernmental Panel on Climate Change (Eds T.F. Stocker, D. Qin, G.-K. Plattner, M. Tignor, S.K. Allen, J. Boschung, A. Nauels, Y. Xia, V. Bex and P.M. Midgley.) pp. 741–866. (Cambridge University Press: Cambridge, UK.)

Flocco, D., Feltham, D. L., and Turner, A. K. (2010). Incorporation of a physically based melt pond scheme into the sea ice component of a climate model. *J. Geophys. Res.-Oceans* **115**, C08012. doi:10.1029/2009JC005568

Flocco, D., Schroeder, D., Feltham, D. L., and Hunke, E. C. (2012). Impact of melt ponds on Arctic sea ice simulations from 1990 to 2007. *J. Geophys. Res.-Oceans* **117**, C09032. doi:10.1029/2012JC008195

Franklin, C. N., Jakob, C., Dix, M., Protat, A., and Roff, G. (2012). Assessing the performance of a prognostic and a diagnostic cloud scheme using single column model simulations of TWP-ICE. *Quart. J. Roy. Meteor. Soc.* **138**, 734–754. doi:10.1002/QJ.954

Ganachaud, A. (2003). Error budget of inverse box models: The North Atlantic. *J. Atmos. Oceanic Technol.* **20**, 1641–1655. doi:10.1175/1520-0426(2003)020<1641:EBOIBM>2.0.CO;2

Ganachaud, A., and Wunsch, C. (2000). The oceanic meridional overturning circulation, mixing, bottom water formation and heat transport. *Nature* **408**, 453–457. doi:10.1038/35044048

Gent, P. R., and McWilliams, J. C. (1990). Isopycnal mixing in ocean circulation models. *J. Phys. Oceanogr.* **20**, 150–155. doi:10.1175/1520-0485(1990)020<0150:IMIOCM>2.0.CO;2

Gent, P. R., Danabasoglu, G., Donner, L. J., Holland, M. M., Hunke, E. C., Jayne, S. R., Lawrence, D. M., Neale, R. B., Rasch, P. J., Vertenstein, M., Worley, P. H., Yang, Z. L., and Zhang, M. (2011). The Community Climate System Model Version 4. *J. Climate* **24**(4973–4991), 2011. doi:10.1175/2011JCLI4083.1

Gregory, D., and Rowntree, P. R. (1990). A massflux convection scheme with representation of cloud ensemble characteristics and stability dependent closure. *Mon. Wea. Rev.* **118**, 1483–1506. doi:10.1175/1520-0493(1990)118<1483:AMFCSW>2.0.CO;2

Gregory, D. and Allen, S. (1991). The effect of convective downdraughts upon NWP and climate simulations. Proceedings of the ninth conference on numerical weather prediction 14–18 October 1991, Denver, Colorado. American Meteorological Society. pp. 122–123.

Gregory, D., Kershaw, R., and Inness, P. M. (1997). Parametrization of momentum transport by convection II: Tests in single-column and general circulation models. *Quart. J. Roy. Meteorol. Soc.* **123**, 1153–1183. doi:10.1002/QJ.49712354103

Griffies, S. M. (2014). Elements of the Modular Ocean Model (MOM) (2012 release with update). GFDL Ocean Group Technical report No. 7, NOAA/GFDL, 632 + xiii pp.

Griffies, S. M., and Hallberg, R. W. (2000). Biharmonic friction with a Smagorinsky viscosity for use in large-scale eddy-permitting ocean models. *Mon. Wea. Rev.* **128**, 2935–2946. doi:10.1175/1520-0493(2000)128<2935:BFWASL>2.0.CO;2

Griffies, S. M., Biastoch, A. W., Boening, C., Bryan, F., Chassignet, E., England, M., Gerdes, R., Haak, H., Hallberg, R. W., Hazeleger, W., Jungclaus, J., Large, W. G., Madec, G., Samuels, B. L., Scheinert, M.,

Gupta, A. S., Severijns, C. A., Simmons, H. L., Treguier, A. M., Winton, M., Yeager, S., and Yin, J. (2009). Coordinated ocean-ice reference experiments (COREs). *Ocean Model* **26**, 1–46. doi:10.1016/J.OCEMOD.2008.08.007

Griffies, S. M., Danabasoglu, G., Durack, P. J., Adcroft, A. J., Balaji, V., Böning, C. W., Chassignet, E. P., Curchitser, E., Deshayes, J., Drange, H., Fox-Kemper, B., Gleckler, P. J., Gregory, J. M., Haak, H., Hallberg, R. W., Heimbach, P., Hewitt, H. T., Holland, D. M., Ilyina, T., Jungclaus, J. H., Komuro, Y., Krasting, J. P., Large, W. G., Marsland, S. J., Masina, S., McDougall, T. J., Nurser, A. J. G., Orr, J. C., Pirani, A., Qiao, F., Stouffer, R. J., Taylor, K. E., Treguier, A. M., Tsujino, H., Uotila, P., Valdivieso, M., Wang, Q., Winton, M., and Yeager, S. G. (2016). OMIP contribution to CMIP6: experimental and diagnostic protocol for the physical component of the Ocean Model Intercomparison Project. *Geosci. Model Dev.* **9**, 3231–3296. doi:10.5194/GMD-9-3231-2016

Harman, I., Bodman, R., Dix, M. and Srbinovsky, J. (2019). CABLE within ACCESS-CM2. CSIRO client report. Available at https://trac.nci.org.au/trac/cable/attachment/wiki/CableDocuments/Harman_2019_CoE_-final_report_revised.pdf.

Hewitt, H. T., Copsey, D., Culverwell, I. D., Harris, C. M., Hill, R. S. R., Keen, A. B., McLaren, A. J., and Hunke, E. C. (2011). Design and implementation of the infrastructure of HadGEM3: the next-generation Met Office climate modelling system. *Geosci. Model Dev.* **4**, 223–253. doi:10.5194/GMD-4-223-2011

Hirst, A. C., Jackett, D. R., and McDougall, T. J. (1996). The meridional overturning cells of a world ocean model in neutral surface coordinates. *J. Phys. Ocean* **26**, 775–791. doi:10.1175/1520-0485(1996)026<0775:TMOCOA>2.0.CO;2

Hunke, E. C., and Dukowicz, J. K. (1997). An Elastic–Viscous–Plastic Model for Sea ice Dynamics. *J. Phys. Oceanogr* **27**(9), 1849–1867. doi:10.1175/1520-0485(1997)027<1849:AEVPMF>2.0.CO;2

Hunke, E. C., Lipscomb, W. H., Turner, A. K., Jeffery, N. and Elliott, S. (2015). CICE: the Los Alamos Sea Ice Model Documentation and Software User's Manual Version 5.1, LA-CC-06-012, Los Alamos National Laboratory, Los Alamos, NM, 2015.

Jochum, M. (2009). Impact of latitudinal variations in vertical diffusivity on climate simulations. *J. Geophys. Res.* **114**, C01010. doi:10.1029/2008JC005030

Jones, P. W. (1997). A User's Guide for SCRIP: A spherical coordinate remapping and interpolation package. LA-CC- 98-45, Los Alamos National Laboratory, N.M.

Kiss, A. E., Hogg, A. McC., Hannah, N., Boeira Dias, F., Brassington, G. B., Chamberlain, M. A., Chapman, C., Dobrohotoff, P., Domingues, C. M., Duran, E. R., England, M. H., Fiedler, R., Griffies, S. M., Heerdegen, A., Heil, P., Holmes, R. M., Klocker, A., Marsland, S. J., Morrison, A. K., Munroe, J., Nikurashin, M., Oke, P. R., Pilo, G. S., Richet, O., Savita, A., Spence, P., Stewart, K. D., Ward, M. L., Wu, F., and Zhang, X. (2020). ACCESS-OM2 v1.0: a global ocean–sea ice model at three resolutions. *Geosci. Model Dev.* **13**, 401–442. doi:10.5194/GMD-13-401-2020

Kowalczyk, E. A., Stevens, L., Law, R. M., Dix, M., Wang, Y. P., Harman, I. N., Hayens, K., Srbinovsky, J., Pak, B., and Zhien, T. (2013). The land surface model component of ACCESS: description and impact on the simulated surface climatology. *Aust. Met. Oceanog. J.* **63**, 65–82. doi:10.22499/2.6301.005

Kuhlbrodt, T., Jones, C. G., Sellar, A., Storkey, D., Blockley, E., Stringer, M., *et al.* (2018). The low-resolution version of HadGEM3 GC3.1: Development and evaluation for global climate. *J. Adv. Model. Earth. Syst.* **10**, 2865–2888. doi:10.1029/2018MS001370

Kwok, R. (2018). Arctic sea ice thickness, volume, and multiyear ice coverage: losses and coupled variability (1958–2018). *Environ, Res, Lett.* **13**, 105005. doi:10.1088/1748-9326/AAE3EC

Large, W., McWilliams, J., and Doney, S. (1994). Oceanic vertical mixing: a review and a model with a nonlocal boundary layer parameterization. *Rev. Geophys.* **32**, 363–403. doi:10.1029/94RG01872

Law, R. M., Ziehn, T., Matear, R. J., Lenton, A., Chamberlain, M. A., Stevens, L. E., Wang, Y.-P., Srbinovsky, J., Bi, D., Yan, H., and Vohralik, P. F. (2017). The carbon cycle in the Australian Community Climate and Earth System Simulator (ACCESS-ESM1) – Part 1: Model description and pre-industrial simulation. *Geosci. Model Dev.* **10**, 2567–2590. doi:10.5194/GMD-10-2567-2017

Lawrence, P. J., Feddema, J. J., Bonan, G. B., Meehl, G. A., O'Neill, B. C., Oleson, K. W., Levis, S., Lawrence, D. M., Kluzek, E., Lindsay, K., and Thorton, P. E. (2012). Simulating the biogeochemical impacts of transient land cover change and wood harvest in the Community Climate System Model (CCSM4) from 1850 to 2100. *J Climate* **25**, 3071–3095. doi:10.1175/JCLI-D-11-00256.1

Lee, H.-C., Rosati, A., and Spelman, M. (2006). Barotropic tidal mixing effects in a coupled climate model: Oceanic conditions in the northern Atlantic. *Ocean Model* **3–4**, 464–477. doi:10.1016/J.OCEMOD.2005.03.003

Leloup, J., Lengaigne, M., and Boulanger, J. (2008). Twentieth century ENSO characteristics in the IPCC database. *Climate Dyn.* **30**, 277C291. doi:10.1007/S00382-007-0284-3

Li, Q., Fox-Kemper, B., Breivikc, Ø., and Webb, A. (2017). Statistical models of global Langmuir mixing. *Ocean Model* **113**(2017), 95–114. doi:10.1016/J.OCEMOD.2017.03.016

Locarnini, R. A., Mishonov, A. V., Antonov, J. I., Boyer, T. P., Garcia, H. E. (2006). 'World Ocean Atlas 2005, Vol. 1: Temperature. NOAA Atlas NESDIS 61'. (U.S. Government Printing Office: Washington, DC.)

Locarnini R. A., Mishonov, A. V., Antonov, J. I., Boyer, T. P. and Garcia, H. E. (2010). 'World Ocean Atlas 2009, Vol. 1: Temperature. NOAA Atlas NESDIS 68'. (U.S. Government Printing Office: Washington DC.)

Lock, A. P. (2001). The numerical representation of entrainment in parametrizations of boundary layer turbulent mixing. *Mon. Wea. Rev.* **129**, 1148–1163. doi:10.1175/1520-0493(2001)129<1148:TNROEI>2.0.CO;2

Lock, A. P., Brown, A. R., Bush, M. R., Martin, G. M., and Smith, R. N. B. (2000). A new boundary layer mixing scheme. Part I: Scheme description and single-column model tests. *Mon. Wea. Rev.* **128**, 3187–3199. doi:10.1175/1520-0493(2000)128<3187:ANBLMS>2.0.CO;2

Lumpkin, R., Speer, K., and Koltermann, K. (2008). Transport across 48°N in the Atlantic Ocean. *J. Phys. Oceanogr.* **38**, 733–752. doi:10.1175/2007JPO3636.1

Mann, G. W., Carslaw, K. S., Spracklen, D. V., Ridley, D. A., Manktelow, P. T., Chipperfield, M. P., Pickering, S. J., and Johnson, C. E. (2010). Description and evaluation of GLOMAP-mode: a modal global aerosol microphysics model for the UKCA composition-climate model. *Geosci. Model Dev.* **3**, 519–551. doi:10.5194/GMD-3-519-2010

Mann, G. W., Carslaw, K. S., Ridley, D. A., Spracklen, D. V., Pringle, K. J., Merikanto, J., Korhonen, S., Schwarz, J. P., Lee, L. A., Manktelow, P. T., Woodhouse, M. T., Schmidt, A., Breider, T. J., Emmerson, K. M., Chipperfield, M. P., and Pickering, S. J. (2012). Intercomparison of modal and sectional aerosol microphysics representations within the same 3-D global chemical transport model. *Atmos. Chem. Phys.* **12**, 4449–4476. doi:10.5194/ACP-12-4449-2012

Manners, J., Edwards, J. M., Hill, P. and Thelen, J.-C. (2015). SOCRATES (Suite Of Community RAdiative Transfer codes based on Edwards and Slingo) Technical Guide, Met Office, UK. Available at https://code.metoffice.gov.uk/trac/socrates (accessed 25 October 2017).

Marsland, S. J., Bi, D., Uotila, P., Fiedler, R., Griffies, S. M., Lorbacher, K., O'Farrell, S., Sullivan, A., Uhe, P., Zhou, X., and Hirst, A. C. (2013). Evaluation of ACCESS climate model ocean diagnostics in CMIP5 simulations. *Aust. Meteor. Oceanogr. J.* **63**, 101–119. doi:10.22499/2.6301.007

McCarthy, G. D., Smeed, D. A., Johns, W. E., Frajka-Williams, E., Moat, B. I., *et al.* (2015). Measuring the Atlantic meridional overturning

circulation at 26°N. *Prog. Oceanogr.* **130**, 91–111. doi:10.1016/J.POCEAN.2014.10.006

Morcrette, C. J. (2012). Improvements to a prognostic cloud scheme through changes to its cloud erosion parametrization. *Atmos. Sci. Let.* **13**, 95–102. doi:10.1002/ASL.374

Murray, R. J. (1996). Explicit generation of orthogonal grids for ocean models. *J. Comput. Phys.* **126**, 251–273. doi:10.1006/JCPH.1996.0136

Naveira Garabato, A. C., McDonagh, E. L., Stevens, D. P., Heywood, K. J., and Sanders, R. J. (2002). On the export of Antarctic BottomWater from the Weddell Sea. *Deep-Sea Research II* **49**, 4715–4742. doi:10.1016/S0967-0645(02)00156-X

Oliver, H., Shin, M., Matthews, D., Sanders, O., Bartholomew, S., Clark, A., Fitzpatrick, B., van Haren, R., Hut, R., and Drost, N. (2019). Workflow Automation for Cycling Systems. *Comput. Sci. Eng.* **21**, 7–21. doi:10.1109/MCSE.2019.2906593

Rayner, N. A., Parker, D. E., Horton, E. B., Folland, C. K., Alexander, L. V., Rowell, D. P., Kent, E. C., and Kaplan, A. (2003). Global analyses of sea surface temperature, sea ice, and night marine air temperature since the late nineteenth century. *J. Geophys. Res.* **108**(No. D14), 4407. doi:10.1029/2002JD002670

Redi, M. H. (1982). Oceanic isopycnal mixing by coordinate rotation. *J. Phys. Oceanogr.* **12**, 1154–1158. doi:10.1175/1520-0485(1982)012<1154:OIMBCR>2.0.CO;2

Ridley, J. K., Blockley, E. W., Keen, A. B., Rae, J. G. L., West, A. E., and Schroeder, D. (2018). The sea ice model component of HadGEM3-GC3.1. *Geosci. Model Dev.* **11**, 713–723. doi:10.5194/GMD-11-713-2018

Samanta, D., Karnauskas, K. B., Goodkin, N. F., Coats, S., Smerdon, J. E., and Zhang, L. (2018). Coupled model biases breed spurious low-frequency variability in the tropical Pacific Ocean. *Geophys. Res. Lett.* **45**, . doi:10.1029/2018GL079455

Shonk, J. K. P., and Hogan, R. J. (2008). Tripleclouds: an efficient method for representing cloud inhomogeneity in 1D radiation schemes by using three regions at each height. *J. Climate* **21**, 2352–2370. doi:10.1175/2007JCLI1940.1

Sillmann, J., Kharin, V. V., Zhang, X., Zwiers, F. W., and Bronaugh, D. (2013). Climate extremes indicesin the CMIP5 multimodel ensemble: Part 1. Model evaluation in the present climate. *J. Geophys. Res. Atmos.* **118**, 1716–1733. doi:10.1002/JGRD.50203

Simmons, H. L., Jayne, S. R., St. Laurent, L. C., and Weaver, A. J. (2004). Tidally driven mixing in a numerical model of the ocean general circulation. *Ocean Model* **6**, 245–263. doi:10.1016/S1463-5003(03)00011-8

Smeed, D. A., Josey, S. A., Beaulieu, C., Johns, W. E., Moat, B. I., Frajka-Williams, E., *et al.* (2018). The North Atlantic Ocean is in a state of reduced overturning. *Geophys. Res. Lett.* **45**, 1527–1533. doi:10.1002/2017GL076350

Stephens, G. L., Hakuba, M. Z., Hawcroft, M., Haywood, J. M., Behrangi, A., Kay, J. E., and Webster, P. J. (2016). The curious nature of the hemispheric symmetry of the Earth's water and energy balances. *Curr. Clim. Change Rep.* **2**(4), 135–147. doi:10.1007/S40641-016-0043-9

Storkey, D., Blaker, A. T., Mathiot, P., Megann, A., Aksenov, Y., Blockley, E. W., Calvert, D., Graham, T., Hewitt, H. T., Hyder, P., Kuhlbrodt, T., Rae, J. G. L., and Sinha, B. (2018). UK Global Ocean GO6 and GO7: a traceable hierarchy of model resolutions. *Geosci. Model Dev.* **11**, 3187–3213. doi:10.5194/GMD-11-3187-2018

Sun, Z., Franklin, C., Zhou, X., Ma, Y., Okely, P., Bi, D., Dix, M., Hirst, A. C., Shonk, J. K. P., and Puri, K. (2013). Modifications in atmospheric physical parameterization for improving SST simulation in the ACCESS coupled model. *Aust. Met. Oceanog. J.* **63**(1), 233–247. doi:10.22499/2.6301.015

Taylor, K. E., Stouffer, R. J., and Meehl, G. A. (2012). An Overview of CMIP5 and the Experiment Design. *Bull. Am. Met. Soc.* **93**(4), 485–498. doi:10.1175/BAMS-D-11-00094.1

Talley, L. D. (2013). Closure of the Global Overturning Circulation Through the Indian, Pacific, and Southern Oceans: Schematics and Transports. *Oceanogr* **26**, 80–97. doi:10.5670/OCEANOG.2013.07

Uotila, P., O'Farrell, S., Marsland, S., and Bi, D. (2012). A sea ice sensitivity study with a global ocean-ice model. *Ocean Model* **51**, 1–18. doi:10.1016/J.OCEMOD.2012.04.002

Valcke, S. (2006). 'OASIS3 User Guide (prism_2-5), PRISM Support Initiative No. 3.' (CERFACS: Toulouse, France.)

Valcke, S., Craig, T., and Coquart, L. (2015). 'OASIS3-MCT User Guide: OASIS3-MCT 3.0, Technical Report, *TR/CMGC/15/38.*' (CERFACS: Toulouse, France.)

Walsh, J. E., Fetterer, F., Stewart, J. S., and Chapman, W. L. (2015). A database for depicting Arctic sea ice variations back to 1850. *Geog. Rev.* **107**, 89–107. doi:10.1111/J.1931-0846.2016.12195.X

Walters, D., Boutle, I., Brooks, M., Melvin, T., Stratton, R., Vosper, S., Wells, H., Williams, K., Wood, N., Allen, T., *et al.* (2017). The Met Office Unified Model Global Atmosphere 6.0/6.1 and JULES Global Land 6.0/6.1 configurations. *Geosci. Model Dev.* **10**, 1487–1520. doi:10.5194/GMD-10-1487-2017

Walters, D., Baran, A. J., Boutle, I., Brooks, M., Earnshaw, P., Edwards, J., Furtado, K., Hill, P., Lock, A., Manners, J., *et al.* (2019). The Met Office Unified Model Global Atmosphere 7.0/7.1 and JULES Global Land 7.0 configurations. *Geosci. Model Dev.* **12**, 1909–1963. doi:10.5194/GMD-12-1909-2019

Watterson, I. W., Hirst, A. C., and Rotstayn, L. D. (2013). A skill-score based evaluation of simulated Australian climate. *Aust. Met. Oceanog. J.* **63**(1), 181–190. doi:10.22499/2.6301.011

West, A. E., McLaren, A. J., Hewitt, H. T., and Best, M. J. (2016). The location of the thermodynamic atmosphere–ice interface in fully coupled models – a case study using JULES and CICE. *Geosci. Model Dev.* **9**, 1125–1141. doi:10.5194/GMD-9-1125-2016

Wilson, D. R., Bushell, A. C., Kerr-Munslow, A. M., Price, J. D., and Morcrette, C. J. (2008). PC2: A prognostic cloud fraction and condensation scheme. I: Scheme description. *Quart. J. Roy. Meteorol. Soc.* **134**, 2093–2107. doi:10.1002/QJ.333

Wood, N., Staniforth, A., White, A., Allen, T., Diamantakis, M., Gross, M., Melvin, T., Smith, C., Vosper, S., Zerroukat, M., and Thuburn, J. (2014). An inherently mass-conserving semi-implicit semi-Lagrangian discretization of the deep-atmosphere global non-hydrostatic equations. *Quart. J. Roy. Meteorol. Soc.* **140**, 1505–1520. doi:10.1002/QJ.2235

Woodward, S. (2011). Mineral dust in HadGEM2, Tech. Rep. **87**. Hadley Centre, Met Office, Exeter, UK

Yu, Y., Maykut, G. A., and Rothrock, D. A. (2004). Changes in thickness distribution of Arctic sea ice between 1958–1970 and 1993–1997. *J. Geophys. Res.* **108**(8), C08004. doi:10.1029/2003JC001982

Zhou, X., Marsland, S., Fiedler, R., Bi, D., Hirst, A. C., and Oscar, A. (2015). Impact of different solar penetration depths on climate simulations. *Tellus A* **67**, 18. doi:10.3402/TELLUSA.V67.25313

Ziehn, T., Chamberlain, M. A., Law, R., Lenton, A., Bodman, R. W., Dix, M., Stevens, L., Wang, Y.-P., and Srbinovsky, J. (2020). The Australian Earth System Model: ACCESS-ESM1.5. *J. South. Hemisph. Earth Syst. Sci.* doi:10.1071/ES19035

Appendix 1. ACCESS-CM2 coupling fields and coupling strategy

Table A1. List of the 2-D coupling fields through OASIS3-MCT in the ACCESS-CM2 system
Fields denoted with * are all defined on 5 ice thickness categories

From UM to CICE (total: 38)	From CICE to UM (total: 46)
1) Total heat flux ($W m^{-2}$)	1) Ocean surface temperature (K)
2) Penetrating solar flux ($W m^{-2}$)	2) Ice-ocean joint velocity (x) ($m s^{-1}$)
3) River runoff ($kg m^{-2} s^{-1}$)	3) Ice-ocean joint velocity (y) ($m s^{-1}$)
4) Wind mixing energy ($W m^{-2}$)	4–8)* Ice concentration (fraction)
5) Rainfall ($kg m^{-2} s^{-1}$)	9–13)* Snow thickness (m)
6) Snowfall ($kg m^{-2} s^{-1}$)	14–18)* Ice thickness (m)
7) Evaporation ($kg m^{-2} s^{-1}$)	The above are the 18 sea ice to atmosphere coupling fields required for the ACCESS1.3 configuration
8) Latent heat flux ($W m^{-2}$)	
9–13)* Top ice melting ($W m^{-2}$)	
14–18)* Bottom ice melting (ice conductive flux)	
19) Windstress (x) ($N m^{-2}$)	
20) Windstress (y) ($N m^{-2}$)	
The above are the legacy fields from the UM7.3 coupling interface, as used in HadGEM3 (r1.1) (Hewitt *et al.* 2011).	
21) Solar radiation net down ($W m^{-2}$)	
22) Longwave radiation net down ($W m^{-2}$)	
23) Sensible heat flux ($W m^{-2}$)	19) CO_2 concentration
24) Surface pressure ($N m^{-2}$)	20) CO_2 flux
These are the 24 fields passed from UM to CICE in ACCESS1.3. Note three of them (No.1, 4 and Nos. 7 or 8) are not really needed.	The above 2 fields are added for ACCESS-ESM1 configuration
25) CO_2 concentration	
26) 10 m height wind speed ($m s^{-1}$)	21) Ocean surface freezing temperature (K)
The above 2 are added for the ACCESS-ESM1 configuration	22–26)* First order ice concentration (fraction)
27) Snow amount over Greenland (kg)	27–31)* Ice top layer temperature (K)
28) Snow amount over Antarctica (kg)	32–36)* Ice top layer effective conductivity ($W m^{-1} deg^{-1}$)
29–33)* Ice skin temperature (K)	37–41)* Ice melt pond concentration (fraction)
34–38)* Ice sublimation rate ($kg m^{-2} s^{-1}$)	42–46)* Ice melt pond thickness (m)

From CICE to MOM (total: 19)	From MOM to CICE (total: 9)
1) Atmosphere/ice-ocean stress (x)	1) Sea surface temperature (K)
2) Atmosphere/ice-ocean stress (y)	2) Sea surface salinity (psu)
3) Rainfall ($kg m^{-2} s^{-1}$)	3) Sea surface water speed (x) ($m s^{-1}$)
4) Snowfall ($kg m^{-2} s^{-1}$)	4) Sea surface water speed (y) ($m s^{-1}$)
5) Salt flux ($kg m^{-2} s^{-1}$)	5) Sea surface gradient (x) (m/m)
6) Ice melt heat flux	6) Sea surface gradient (y) (m/m)
7) Shortwave penetrating into ocean ($W m^{-2}$)	7) Potential ice form/melt heat flux ($W m^{-2}$)
8) Latent heat flux ($W m^{-2}$)	These are the 7 fields passed from MOM into CICE in ACCESS1.3.
9) Sensible heat flux ($W m^{-2}$)	(Note the sea surface gradient is supposed to be used for calculation of ocean-sea stress due to sea surface slope but it is too noisy and causes instability of the model. Therefore, in practice (for both ACCESS1.3 and ACCESS-CM2) a geostrophic estimation is applied for this purpose by using the mean ocean current speed.)
10) Longwave radiation ($W m^{-2}$)	
11) Runoff ($kg m^{-2} s^{-1}$)	
12) Pressure (Pa)	
13) Ice concentration (fraction)	
Above are the all CICE to MOM fields in ACCESS1.3.	
14) Ice melt water flux ($kg m^{-2} s^{-1}$)	8) CO_2
15) Ice form water flux ($kg m^{-2} s^{-1}$)	9) CO_2 flux
These two are added for ACCESS1.4 (the physical core of ACCESS-ESM1)	The above 2 fields are required for ACCESS-ESM1.
16) CO_2	
17) 10 m height wind speed ($m s^{-1}$)	
The above 2 are added for ACCESS-ESM1	
18) Iceberg calving water flux ($kg m^{-2} s^{-1}$)	
19) Iceberg calving heat flux ($W m^{-2}$)	

A1 Coupling strategy

In ACCESS1.3, with zero-layer thermodynamics for the sea ice, the surface exchange fluxes are calculated for a single sea ice category. In ACCESS-CM2, however, the ice-atmosphere coupling is undertaken by ice thickness category, namely, the surface exchange fluxes are calculated separately for each of the 5 ice thickness categories, as well as for open water. In addition, although the melt-pond evolution is calculated in CICE, the pond fraction and thickness are required by JULES for its surface exchange scheme to determine surface albedo.

Following the practice in HadGEM-GC3.1, energy flux passing from UM to CICE in ACCESS-CM2 is conducted with a "semi-implicit" coupling algorithm as described in Ridley *et al.* (2018) for energy conservation. However, unlike the HadGEM-GC3.1 model that uses second-order conservative regridding of selected fields for smoothing the data passing the coupler, ACCESS-CM2 only uses first-order conservative remapping algorithm of the Spherical Coordinate Remapping and Interpolation Package (SCRIP) (Jones 1997) for UM-CICE coupling. It is known that, when the grids of two models of coupling are markedly different (e.g. in shape and resolution), there appears to have imprint of the coarser resolution grid seen in some fields remapped onto the finer grid. Second order conservative regridding is proven to reduce such imprint only if the fields to be remapped are already relatively smooth, but it may also increase the noise in fields. We have chosen not to use second order regridding at this time based on the judgement that the UM N96 grid and the 1-degree ocean grid used for ACCESS-CM2 are not so different in terms of resolution, and on the fact that second order conservative regridding requires extra data (gradient of the fields) exchanged and largely increases the complexity of coupling. In addition, some second-order conservative methods can produce spurious extrema, including small negative values of fluxes (such as rainfall or shortwave radiation) that should only be positive.

Two newly added "coupling fields" for ACCESS-CM2, the total amount of snow on land ice over Greenland and Antarctica, are worth being described here in some detail because of their importance in maintaining hydrological balance of the system. For data passing purpose, they are defined as 2-D fields but contain a uniform value, the accumulated snow amount on land ice over Greenland and Antarctica, respectively. They are required for the coupling because the current UM-JULES configuration allows an unphysical free accumulation of snow on land ice, and this continuous increment must be returned to the ocean to balance the water loss there. In reality, the balance would be achieved through run off and iceberg calving. In ACCESS-CM2, once the increment of snow on land ice in the NH and SH (over the UM-CICE coupling interval) is calculated, this quantity is passed from the UM into CICE. Then we use a simplified scheme based on Storkey *et al.* (2018) to convert this increment into 2-D water and heat fluxes around Greenland and Antarctica, following the geographical distribution pattern of iceberg calving climatology (D. Storkey, pers. comm.). The water and heat fluxes are then passed to MOM.